J. Fluid Mech. (2011), *vol.* 677, *pp.* 503–529.
doi:10.1017/jfm.2011.97

Channel and shoal development in a short tidal embayment: an idealized model study

MIRIAM C. TER BRAKE† AND HENK M. SCHUTTELAARS
Delft Institute of Applied Mathematics, TU Delft, Mekelweg 4, Delft 2628CD, The Netherlands

(Received 28 June 2010; revised 16 February 2011; accepted 20 February 2011;
first published online 3 May 2011)

In many tidal embayments, complex patterns of channels and shoals are observed. To gain a better understanding of these features, an idealized model, that describes the interaction of water motion, sediment transport and bed evolution in a semi-enclosed, rectangular basin, is developed and analysed. To explain the initial formation of channels and shoals, two-dimensional perturbations superposed on a laterally uniform equilibrium bottom are studied. These perturbations evolve due to convergences of various residual suspended sediment fluxes: a diffusive flux, a flux related to the bed topography, an advective flux resulting from internally generated overtides and an advective flux due to externally prescribed overtides. For most combinations of these fluxes, perturbations start to grow if the bottom friction is strong enough. Their growth is mainly a result of convergences of diffusive and topographically induced sediment fluxes. Advective contributions due to internally generated overtides enhance this growth. If only diffusive sediment fluxes are considered, the underlying equilibrium is always unstable. This can be traced back to the depth dependence of the deposition parameter. Contrary to the results of previous idealized models, the channels and shoals always initiate in the shallow, landward areas. This is explained by the enhanced generation (compared to that in previous models) of frictional torques in shallow regions. The resulting initial channel–shoal formation compares well with results found in complex numerical model studies. The instability mechanism and the location of the initial formation of bottom patterns do not change qualitatively when varying parameters. Changes are mainly related to differences in the underlying equilibrium profile due to parameter variations.

Key words: coastal engineering, morphological instability, pattern formation

1. Introduction

Tide-dominated embayments are important features of many coastal systems. Examples of such systems are found along the Dutch, German and Danish Wadden coast (Ehlers 1988; Davis 1996). Their morphology is often complex, exhibiting patterns of deep channels separated by shallow, sandy shoals. Usually, the depth of the channels decreases and the number of channels increases in the landward direction.

An example of such an embayment in the Dutch Wadden Sea is the Ameland Inlet system, located between the Dutch barrier islands Terschelling and Ameland (see figure 1). The width of this inlet is ∼2 km, its length is ∼19 km and the averaged

† Email address for correspondence: miriam.terbrake@bmtargoss.com

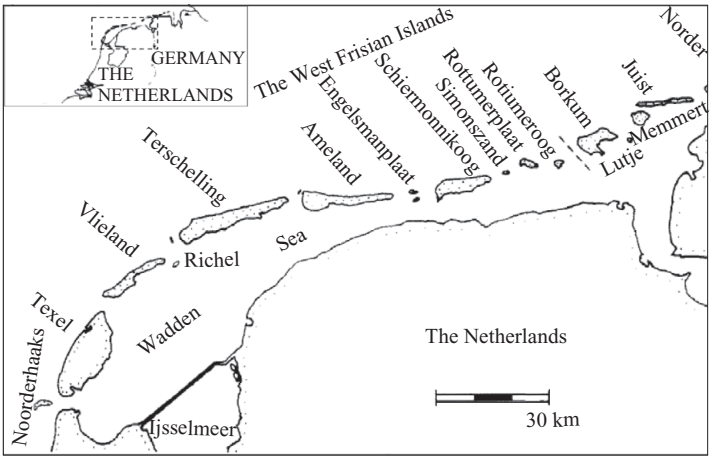

FIGURE 1. Tidal inlet systems in the Dutch Wadden Sea (after Sha 1989). The Amelander Inlet system is located between the barrier islands Terschelling and Ameland.

depth at the entrance is ∼12 m. The water motion in this area is dominated by a semidiurnal tide with a mean tidal amplitude of ∼1 m. The channels form a large-scale *fractal* pattern (Cleveringa & Oost 1999).

Recently, complex process-based morphodynamic models were able to simulate the development of channel–shoal systems in tidal basins (Marani *et al.* 2003; Marciano *et al.* 2005; Roelvink 2006; D'Alpaos *et al.* 2007) and tidal inlets (Hibma, de Vriend & Stive 2003; Hibma, Schuttelaars & de Vriend 2004; van der Wegen & Roelvink 2008; Dissanayake, Roelvink & van der Wegen 2009). For example, van der Wegen & Roelvink (2008) simulated bed evolution in a short tidal embayment, starting from a constantly sloping, laterally uniform bed profile. Initially channels and shoals developed in the relatively shallow landward end of the embayment. The number of channels and shoals in the embayment increased with increasing embayment width. Obviously, these numerical models include the main physical mechanisms for the formation of channel–shoal systems. However, they are too complex to determine which mechanism is essential for the behaviour of the simulated phenomena.

To elucidate the physical mechanisms resulting in the observed development of channels and shoals, idealized models were devised. As a first step, Schuttelaars & de Swart (1996) and van Leeuwen, Schuttelaars & de Swart (2000) developed cross-sectionally averaged models for short embayments (for an extensive overview, see de Swart & Zimmerman 2009). Considering only a prescribed M_2 tidal elevation at the entrance of the embayment, a unique morphodynamic equilibrium was found, characterized by a constantly sloping bed. If both the M_2 and the M_4 tidal constituents were considered, van Leeuwen *et al.* (2000) obtained equilibrium profiles that were strongly convex and much shorter than those found in observations. This motivated ter Brake & Schuttelaars (2010) to investigate the influence of the vertical distribution of suspended sediment on width-averaged equilibrium profiles. They found that when the vertical distribution was included, morphodynamic equilibria could be found with embayment lengths similar to those observed in the Dutch Wadden Sea.

To address channel–shoal formation, the linear stability of these cross-sectionally averaged morphodynamic equilibria has to be investigated. This was first done

by Schuttelaars & de Swart (1999), who studied the linear stability of laterally uniform morphodynamic equilibria by perturbing them with small, two-dimensional disturbances. Sediment was transported by diffusive processes and local bed slope terms. It was found that the basic state was unstable if the friction parameter exceeded a critical value. The maximum amplitude of the bed perturbation was found in the middle of the tidal embayment. van Leeuwen & de Swart (2001, 2004) extended this model by retaining internally generated advective contributions. They found that bars were formed near the seaward boundary if the sediment transport was dominated by advective processes. Diffusively dominated transport resulted in bed forms located more towards the centre of the embayment. Compared to the results found in complex numerical model simulations (van der Wegen & Roelvink 2008), the location where the initial bed forms are observed is very different: in the idealized models the initial bed forms are located in the seaward section, while in the numerical modelling studies they are found near the landward boundary. Apart from this difference, the idealized model studies do not consider a prescribed external overtide or the effects of the vertical suspended sediment distribution on the stability of bed perturbations, even though they strongly influence existence and characteristics of the underlying laterally uniform morphodynamic equilibria (ter Brake & Schuttelaars 2010).

In view of these observations, the present paper aims to answer the following questions. First, what is the influence of the various sediment fluxes on the linear stability properties of two-dimensional perturbations on the cross-sectionally averaged morphodynamic equilibria presented in ter Brake & Schuttelaars (2010)? There will be a particular focus on the topographically induced sediment flux (i.e. the flux related to the vertical distribution of suspended sediment) and the flux that is driven by external overtides. Second, what controls the location where the most unstable perturbations in the embayment are found? And finally, how sensitive are these results to variations in parameter values, such as the grain size, the external overtide and the bottom friction parameterization?

These questions will be answered by performing a linear stability analysis. First the physical model is described in § 2, followed by a short description of the basic state and a derivation of the eigenvalue problem (§ 3). The results of the default experiment and the influence of different flux contributions are presented in § 4. These results are extensively discussed in § 5, where the instability mechanism is described. The location of the initial formation of the bed patterns is explained and model sensitivities are discussed. In § 6, conclusions are drawn.

2. Model formulation

2.1. *Geometry*

The geometry considered is that of a semi-enclosed rectangular basin with constant width B, tidally averaged length L and prescribed water depth H at the entrance. At the landward side of the embayment the local water depth $H - h + \zeta$ vanishes. Here ζ is the sea surface elevation above $z = H$ and h is the bed level above a horizontal datum at $z = 0$. The sidewalls at $y = 0, B$ are assumed to be fixed and the bed is erodible, see figure 2. It is assumed that the bottom of the embayment consists of uniform fine sand with a typical grain size $d \sim 130\,\mu\text{m}$, that can be transported as suspended load or bedload.

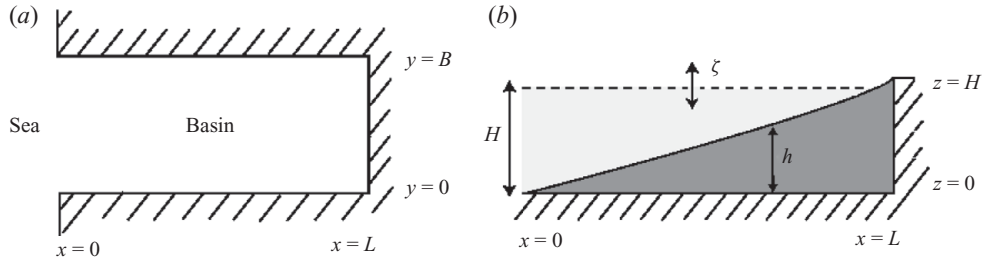

FIGURE 2. (*a*) Top view and (*b*) cross-sectional view of the embayment. For an explanation of the symbols, see the text.

2.2. *Hydrodynamics*

The water motion is described by the two-dimensional depth-averaged shallow water equations (Vreugdenhil 1994)

$$\zeta_t + [(\zeta + H - h)u]_x + [(\zeta + H - h)v]_y = 0, \tag{2.1}$$

$$u_t + uu_x + vu_y = -g\zeta_x - \frac{\tau_{b1}}{\rho_s(\zeta + H - h + h_0)}, \tag{2.2}$$

$$v_t + uv_x + vv_y = -g\zeta_y - \frac{\tau_{b2}}{\rho_s(\zeta + H - h + h_0)}. \tag{2.3}$$

As narrow and relatively shallow estuaries are considered, Coriolis effects are neglected. No freshwater inflow is considered, which allows for the neglect of density effects. From scaling arguments it follows that Reynolds stresses, related to turbulent mixing of momentum in the horizontal direction, are negligible. As a first step, no wind effects are taken into account. The variables u and v represent depth-averaged velocities in the longitudinal and lateral directions, respectively. Furthermore, t is time, g is the acceleration due to gravity and ρ_s is the density of sediments (2650 kg m^3). The last contributions on the right-hand side of (2.2) and (2.3) are the bed shear stresses, divided by the local water depth. A constant h_0 is introduced to keep the bottom friction finite even if the water depth goes to zero. Following Zimmerman (1982), a linearized formulation of the bed shear stress (τ_{b1},τ_{b2}) is used:

$$\tau_{b1} = \rho_s r^* u, \quad \tau_{b2} = \rho_s r^* v, \tag{2.4}$$

where r^* is a friction coefficient with dimensions m s^{-1}. The parameter r^* is chosen such that the net dissipation of energy (averaged over a tidal cycle and over the embayment) due to the linearized stress equals that of the bed shear stress based on the quadratic friction law. It is shown by Schramkowski, Schuttelaars & de Swart (2002) that this linearization of the bottom stress only marginally affects the morphodynamics of tidal embayments.

At the entrance, the sea surface elevation is prescribed and consists of an M_2 and an M_4 tidal constituent. At the landward side the kinematic boundary condition is used and at the sidewalls (i.e. $y = 0$ and $y = B$) the water flux vanishes. Explicit expressions for these boundary conditions will be discussed in more detail in § 2.4.

2.3. *Sediment transport and bed evolution*

The concentration of suspended sediment and the evolution of the bottom are described by the two-dimensional equivalents of the equations, used in ter Brake &

Schuttelaars (2010). For details, we refer to this article. The resulting equations read

$$C_t + \left[uC - \tilde{\kappa}C_x - \tilde{\kappa}\frac{\omega_s}{\kappa_v}\beta h_x C\right]_x + \left[vC - \tilde{\kappa}C_y - \tilde{\kappa}\frac{\omega_s}{\kappa_v}\beta h_y C\right]_y = \alpha(u^2+v^2) - \frac{\omega_s^2}{\kappa_v}\beta C, \tag{2.5a}$$

$$\rho_s(1-p)\left[h_t + \mu\nabla^2(h-h_{eq})\right] = -\left\langle \alpha(u^2+v^2) - \frac{\omega_s^2}{\kappa_v}\beta C\right\rangle. \tag{2.5b}$$

Here C is the depth-integrated sediment concentration, $\tilde{\kappa}$ is the horizontal diffusivity ($\sim 10^2\,\mathrm{m}^2\,s^{-1}$), κ_v is the vertical diffusivity ($\sim 0.1\,\mathrm{m}^2\,s^{-1}$), ω_s is the settling velocity ($\sim 0.015\,\mathrm{m\,s}^{-1}$), α is an erosion constant ($\sim 10^{-4}\,\mathrm{kg\,m}^{-2}\,\mathrm{s}^{-1}$) which depends on the sediment characteristics and β is the deposition parameter:

$$\beta = \left[1 - \exp\left(-\frac{\omega_s}{\kappa_v}(\zeta + H - h)\right)\right]^{-1}. \tag{2.6}$$

Furthermore, $\nabla = (\partial/\partial x, \partial/\partial y)$, h_{eq} is a width-averaged equilibrium bottom profile (specified in § 3), $p \sim 0.4$ is the porosity of sediment and μ ($\sim 10^{-6}$–$10^{-4}\,\mathrm{m}^2\,s^{-1}$) determines the magnitude of the bedload contribution proportional to the local bedslope.

As boundary conditions at the entrance, the bed level h is fixed ($h = 0$) and there is a tidally averaged balance between erosion and deposition,

$$\left\langle \alpha(u^2+v^2) - \frac{\omega_s^2}{\kappa_v}\beta C\right\rangle = 0 \quad \text{at } x = 0, \tag{2.7}$$

The boundary conditions at the sidewalls require a vanishing suspended load and bedload sediment flux:

$$vC - \tilde{\kappa}C_y - \tilde{\kappa}\frac{\omega_s}{\kappa_v}\beta h_y C = 0 \quad \text{and} \quad h_y = 0 \quad \text{at } y = 0, B. \tag{2.8}$$

At the landward side, we require the water depth to vanish at $\hat{x}(x, y)$. Here, $\hat{x}(x, y)$ is the position of the moving water front (with the tidally averaged longitudinal coordinate of $\langle\hat{x}\rangle = L$). Apart from this condition, the tidally averaged sediment flux has to vanish at the moving boundary:

$$\rho_s(1-p)\mu\nabla(h-h_{eq})\cdot\boldsymbol{n} + \left\langle -\tilde{\kappa}\nabla C - \tilde{\kappa}\frac{\omega_s}{\kappa_v}\beta\nabla h C\right\rangle\cdot\boldsymbol{n} = 0 \quad \text{at } x = \hat{x}(x, y), \tag{2.9}$$

where $\boldsymbol{n}$ is the normal vector.

2.4. *Scaling and derivation of the short-embayment model*

The governing equations are made dimensionless by introducing characteristic scales for the physical variables. Dimensionless parameters, shown below, are denoted with an asterisk *:

$$\left.\begin{aligned} &u = Uu^*, \quad v = Uv^*, \quad C = \frac{\alpha U^2\kappa_v}{\omega_s^2}C^*, \quad \zeta = A_{M_2}\zeta^*, \quad h = Hh^*, \quad t = \sigma^{-1}t^*,\\ &x = Lx^*, \quad y = Ly^*, \quad \beta = \beta^*, \quad r = \frac{H}{\sigma}r^*, \quad \mu = \sigma L^2\mu^*, \end{aligned}\right\} \tag{2.10}$$

The characteristic scales include the tidally averaged length L of the basin, the reference depth H at the entrance of the embayment and the free surface amplitude

A_{M_2}. The velocity scale follows from the continuity equation and reads $U = \sigma A_{M_2} L/H$. The typical scale for the concentration is obtained by requiring an approximate balance between erosion and deposition.

After suppressing the asterisk of the dimensionless variables, the dimensionless equations for the water motion become

$$\zeta_t + [(\epsilon\zeta + 1 - h)u]_x + [(\epsilon\zeta + 1 - h)v]_y = 0, \tag{2.11}$$

$$\lambda_L^2 \left[u_t + \epsilon(uu_x + vu_y) + \frac{r}{(\epsilon\zeta + 1 - h + h_0)} u \right] = -\zeta_x, \tag{2.12}$$

$$\lambda_L^2 \left[v_t + \epsilon(uv_x + vv_y) + \frac{r}{(\epsilon\zeta + 1 - h + h_0)} v \right] = -\zeta_y. \tag{2.13}$$

Here ϵ is the ratio of the tidal excursion length U/σ and the embayment length L, and $\lambda_L = \sigma L/\sqrt{gH}$ is, apart from a factor of 2π, the ratio of the embayment length and the frictionless tidal wavelength $L_g = T\sqrt{gH}$.

Assuming that bottom friction is only moderate (i.e. frictional terms in the momentum equation are of the same order as the local acceleration terms) and considering only short embayments (i.e. the length L is assumed to be small compared to the frictionless tidal wavelength L_g, resulting in $\lambda_L \ll 1$), the momentum equations reduce in lowest order to

$$\zeta_x = 0 \quad \text{and} \quad \zeta_y = 0. \tag{2.14}$$

Hence, the free surface elevation is spatially uniform. This condition and the width-averaged equivalent of condition (2.11) were used by ter Brake & Schuttelaars (2010) to solve for the cross-sectionally averaged velocity u and ζ. However, in case the equations are only averaged over the depth, (2.11) and (2.14) are not sufficient to solve for both the velocities u and v. To close the system of equations, we eliminate the pressure terms from (2.12) and (2.13) by taking cross-derivatives of the full momentum equations (i.e. get the y-derivative of (2.12) and the x-derivative of (2.13)), and subtracting the results. This results in the vorticity equation

$$\Omega_t + \epsilon[(u\Omega)_x + (v\Omega)_y] = \left[\frac{ru}{(\epsilon\zeta + 1 - h + h_0)} \right]_y - \left[\frac{rv}{(\epsilon\zeta + 1 - h + h_0)} \right]_x, \tag{2.15}$$

with $\Omega = v_x - u_y$ the relative vorticity. The terms on the left-hand side of (2.15) represent the local change of relative vorticity and the divergence of the vorticity flux. The terms on the right-hand side model the dissipation of vorticity by bottom friction, as well as vorticity production by bottom frictional torques. In previous studies by Schuttelaars & de Swart (1996) and van Leeuwen *et al.* (2000), the contribution on the right-hand side (with $h_0 = 0$) was linearized with respect to the local water depth, assuming that $h - \epsilon\zeta \ll 1$ everywhere in the tidal inlet. Only the first two terms in the Taylor expansion were retained as this already resulted in the generation of vorticity. In this work we do not linearize these contributions but introduce a parameter $h_0 > 0$ to ensure that the bottom friction remains bounded if the water depth goes to zero. A similar approach to regularize the bottom friction has already been applied by Schuttelaars & de Swart (2000) and Schuttelaars, Schramkowski & de Swart (2001).

The dimensionless concentration equation (2.5*a*) becomes

$$a\{C_t + (\epsilon uC - \kappa[C_x + \lambda\beta h_x C])_x + (\epsilon vC - \kappa[C_y + \lambda\beta h_y C])_y\} = u^2 + v^2 - \beta C, \tag{2.16}$$

Channel	Tide	Sediment	Dimensionless
$L = 19 \times 10^3$ m	$A_{M_2} = 0.84$ m	$\omega_s = 0.015$ m s^{-1}	$\epsilon = \dfrac{U}{\sigma L} = \dfrac{A_{M_2}}{H} \sim 0.07$
$H = 12$ m	$A_{M_4} = 0.08$ m	$\kappa_v = 0.1$ m^2 s^{-1}	$\kappa = \dfrac{\tilde{\kappa}}{\sigma L^2} \sim 1.79 \times 10^{-3}$
$B = 2 \times 10^3$ m	$\sigma = 1.4 \times 10^{-4}$ s^{-1}	$\alpha = 10^{-2}$ kg s m^{-4}	$a = \dfrac{\sigma \kappa_v}{\omega_s^2} \sim 0.0622$
	$\phi = 195^\circ$	$\tilde{\kappa} = 10^2$ m^2 s^{-1}	$\lambda = \dfrac{\omega_s}{\kappa_v} H \sim 1.8$
		$p = 0.4$	$\gamma = 2\dfrac{A_{M_4}}{A_{M_2}} \sim 0.19$
		$\rho_s = 2650$ kg m^3	$\delta = \dfrac{\alpha U^2}{\sigma H \rho_s (1-p)} \sim 1.3 \times 10^{-5}$
		$h_0 = 0.4$	$r = r^*/\sigma H \sim 10^{-3}/1.68 \times 10^{-3}$
			$\mu = \sigma L^2 \mu^* \sim 3.4 \times 10^{-6}$

TABLE 1. Characteristic values for the Ameland Inlet system.

with a the ratio of the deposition time scale over the tidal time scale, κ the non-dimensional horizontal diffusion parameter and λ the sediment Péclet number, which is the ratio of the typical time it takes a particle to settle in the water column and the typical time needed to mix particles through the water column (for a definition of the dimensionless parameters, see table 1). The dimensionless deposition parameter β reads $\{1 - \exp[-\lambda(\epsilon\zeta + 1 - h)\}^{-1}$.

Finally, the scaled bottom evolution equation is given by

$$h_\tau = -\langle \nabla \cdot \boldsymbol{F} \rangle, \tag{2.17}$$

where $\tau = \delta t$ is the slow morphodynamic time, with $\delta = \alpha U^2/(\sigma H \rho_s (1-p))$. The vector $\boldsymbol{F} = (F^1, F^2)$ denotes the sediment flux, with components given by

$$F^1 = a[\epsilon u C - \kappa[C_x + \lambda \beta h_x C]] + \mu(h_x - h_{eq,x}), \tag{2.18}$$

$$F^2 = a[\epsilon v C - \kappa[C_y + \lambda \beta h_y C]] + \mu(h_y - h_{eq,y}). \tag{2.19}$$

The first contribution to both F^1 and F^2 represents the advective sediment flux and the second one the diffusive flux. The third contribution models the topographically induced suspended sediment transport and the last term the bedload transport related to the local bedslope.

At the entrance, the scaled sea surface elevation ζ is prescribed as $\zeta = \cos(t) + \gamma \cos(2t - \phi)/2$ with γ the ratio of the tidal amplitudes of the M_4 and M_2 tidal constituents. The phase difference ϕ is defined as the difference between the phases of these constituents, $\phi_{M_4} - 2\phi_{M_2}$, where ϕ_{M_2} and ϕ_{M_4} are the phases of the M_2 and M_4 tidal constituents at the entrance. Using the momentum equation (2.13) and the reduced momentum equation (2.14), it follows that $v_t + \epsilon u v_x + \epsilon v v_y = -rv/(\epsilon\zeta + 1 + h_0)$ at $x = 0$. Concerning the concentration at the entrance, it is required that erosion and deposition balance over a tidal cycle ($\langle u^2 + v^2 - \beta C \rangle = 0$) and that no diffusive boundary layer develops for the time-varying part ($\tilde{C}(x, y, t, \kappa) = \tilde{C}(x, y, t, \kappa = 0)$). Furthermore, the bed is fixed at the entrance ($h = 0$).

The boundary conditions at the moving landward end ($x = \hat{x}$) are reformulated as the conditions at the averaged landward boundary $x = 1$. Following van Leeuwen & de Swart (2001) it is found that in leading order $h = 1$ at $x = 1$. Substituting this condition into the continuity equations and noting that the derivatives of

ζ are zero (2.14), it follows that $\zeta_t - h_x u + \epsilon\zeta u_x - h_y v + \epsilon\zeta v_y = 0$. Furthermore, we require that the tidally averaged flux $\langle F^1 \rangle = 0$ and that no diffusive boundary layer develops for the time-fluctuating part of the suspended sediment concentration, $\tilde{C}(x, y, t, \kappa) = \tilde{C}(x, y, t, \kappa = 0)$.

The scaled boundary condition at the walls requires the water flux $(1 - h_\epsilon \zeta)v$ to vanish. Furthermore, both the suspended load flux $\epsilon v C - \kappa(C_y + \beta h_y C)$ and the bedload flux $\mu(h - h_{eq})_y$ have to vanish as well.

3. Basic state and linear stability analysis

ter Brake and Schuttelaars (2010) showed that the system of equations, specified in § 2.4, allows for morphodynamic equilibria that are uniform in the lateral direction. However, it is not clear if these morphodynamic equilibria are stable with respect to small bottom perturbations that vary over the width. To investigate the linear stability of these equilibria, small two-dimensional perturbations are superimposed on the basic state:

$$\boldsymbol{\Psi}(x, y, t, \tau) = \boldsymbol{\Psi}_{eq}(x, t) + \boldsymbol{\Psi}'(x, y, t), \tag{3.1}$$

where $\boldsymbol{\Psi} = (u, v, \zeta, C, h)$. The subscript (eq) denotes the one-dimensional basic state and the prime indicates any small two-dimensional perturbations. To investigate the linear stability of a morphodynamic equilibrium, $\boldsymbol{\Psi}$ is substituted into the original system of equations and linearized around the equilibrium solution (i.e. contributions to the equations that are nonlinear in the small perturbations are neglected). The resulting system of equations is presented in Appendix A.

The equations and boundary conditions presented in Appendix A allow for solutions of the form

$$\left.\begin{aligned} u' &= \mathrm{Re}\{\hat{u}_n(x, t)\cos(l_n y)\,\mathrm{e}^{\omega\tau}\}, \quad v' = \mathrm{Re}\{\hat{v}_n(x, t)\sin(l_n y)\,\mathrm{e}^{\omega\tau}\}, \\ C' &= \mathrm{Re}\{\hat{C}_n(x, t)\cos(l_n y)\,\mathrm{e}^{\omega\tau}\}, \quad h' = \mathrm{Re}\{\hat{h}_n(x)\cos(l_n y)\,\mathrm{e}^{\omega\tau}\}. \end{aligned}\right\} \tag{3.2}$$

Here Re denotes the real part of the solution, and l_n is the dimensionless lateral wavenumber of the perturbation, defined as

$$l_n = n\pi L/B, \quad n = 0, 1, 2, \ldots, \tag{3.3}$$

with n the lateral mode number. The complex number ω follows from an eigenvalue problem (see (3.11)), with its real part denoting the exponential growth rate of the perturbation. The migration rate is given by its imaginary part $\mathrm{Im}(\omega)$. If $\mathrm{Re}(\omega) > 0$, the morphodynamic equilibrium is unstable and the amplitude of the perturbations grows exponentially in time.

Following the solution method for the basic state (ter Brake & Schuttelaars 2010), the variables that depend on the tidal time scale are expanded with respect to the small parameters ϵ and γ (defined in table 1):

$$\hat{\chi}_n(x, t) = \hat{\chi}_n^{0,0}(x, t) + \epsilon\hat{\chi}_n^{1,0}(x, t) + \gamma\hat{\chi}_n^{0,1}(x, t) + \cdots, \tag{3.4}$$

with $\hat{\chi}_n$ any of the variables $\hat{u}_n$, $\hat{v}_n$ and $\hat{C}_n$. The first superscript gives the order in ϵ and the second one the order in γ. The subscript n denotes the lateral wavenumber. These expansions are substituted in the linearized system of equations (presented in Appendix A) and terms of equal powers of ϵ and γ are collected.

From the leading-order system of equations (i.e. independent of ϵ and γ) and the boundary conditions, it follows that the leading-order solutions can be written as

$$\hat{u}_n^{0,0}(x,t) = u_{n,s}^{0,0}(x)\sin(t) + u_{n,c}^{0,0}(x)\cos(t), \tag{3.5a}$$

$$\hat{v}_n^{0,0}(x,t) = v_{n,s}^{0,0}(x)\sin(t) + v_{n,c}^{0,0}(x)\cos(t), \tag{3.5b}$$

$$\hat{C}_n^{0,0}(x,t) = \left\langle C_n^{0,0}(x)\right\rangle + C_{n,s2}^{0,0}(x)\sin(2t) + C_{n,c2}^{0,0}(x)\cos(2t), \tag{3.5c}$$

where $\langle\cdot\rangle$ denotes a tidally averaged contribution. The first subscript of the amplitude is the lateral wavenumber and the second subscript is the tidal constituent under consideration: s (c) denotes a sine (cosine) tidal constituent with M_2 tidal frequency, $s2$ ($c2$) a sine (cosine) constituent with M_4 tidal frequency. The meaning of the superscripts was previously discussed below (3.4). Substitution of these expressions in the leading-order system of equations results in ordinary differential equations that describe the leading-order water motion and suspended sediment concentration (see Appendix B).

The order ϵ velocity components $\hat{u}_n^{1,0}$ and $\hat{v}_n^{1,0}$ result from advective and bottom friction contributions in the vorticity equation and the nonlinear terms in the continuity equation. Using the temporal and spatial structure of the zeroth-order solution, it follows that these components consist of a residual contribution and contributions that vary with twice the basic tidal frequency. The concentration $\hat{C}_n^{1,0}$ consists of an M_2 and an M_6 contribution. Since the M_6 constituent does not contribute to the leading-order sediment transport, we will not consider this contribution in the remainder. The expressions for the solutions of the $O(\epsilon)$ system of equations read

$$\hat{u}_n^{1,0}(x,t) = \left\langle u_n^{1,0}(x)\right\rangle + u_{n,s2}^{1,0}(x)\sin(2t) + u_{n.c2}^{1,0}(x)\cos(2t), \tag{3.6a}$$

$$\hat{v}_n^{1,0}(x,t) = \left\langle v_n^{1,0}(x)\right\rangle + v_{n,s2}^{1,0}(x)\sin(2t) + v_{n,c2}^{1,0}(x)\cos(2t), \tag{3.6b}$$

$$\hat{C}_n^{1,0}(x,t) = C_{n,s}^{1,0}(x)\sin(t) + C_{n,c}^{1,0}(x)\cos(t). \tag{3.6c}$$

Substitution of these expressions results in the equations presented in Appendix B.

The externally prescribed overtide results in order γ contributions $\hat{u}_n^{0,1}$, $\hat{v}_n^{0,1}$ and $\hat{C}_n^{0,1}$. The velocity fields $\hat{u}_n^{0,1}$ and $\hat{v}_n^{0,1}$ consist of tidal constituents with M_4 frequency, and the concentration $\hat{C}_n^{0,1}$ consists of an M_2 and an M_6 contribution. Again neglecting the M_6 contribution, the solutions of the $O(\gamma)$ system of equations can be written as

$$\hat{u}_n^{0,1}(x,t) = u_{n,s2}^{0,1}(x)\sin(2t) + u_{n,c2}^{0,1}(x)\cos(2t), \tag{3.7a}$$

$$\hat{v}_n^{0,1}(x,t) = v_{n,s2}^{0,1}(x)\sin(2t) + v_{n,c2}^{0,1}(x)\cos(2t), \tag{3.7b}$$

$$\hat{C}_n^{0,1}(x,t) = C_{n,s}^{0,1}(x)\sin(t) + C_{n,c}^{0,1}(x)\cos(t). \tag{3.7c}$$

The resulting equations for the new unknowns are given in Appendix B.

Finally the bottom evolution equation has to be considered. Substituting the expressions for velocity and concentration fields presented above, retaining only the leading-order contributions in ϵ and γ (i.e. $O(\epsilon^2)$ and $O(\epsilon\gamma)$ terms) and the diffusive contributions, the perturbed sediment flux can be written as

$$\boldsymbol{F}' = [\mathrm{Re}\{F^{1'}\cos(l_n y)\,\mathrm{e}^{\omega\tau}\}, \mathrm{Re}\{F^{2'}\sin(l_n y)\,\mathrm{e}^{\omega\tau}\}], \tag{3.8}$$

with $F^{i'}$, $i \in \{1, 2\}$, given by

$$F^{i'} = F^{i'}{}_{diff} + F^{i'}{}_{vd} + F^{i'}{}_{bl} + F^{i'}{}_{int} + F^{i'}{}_{ext}. \tag{3.9}$$

Experiment	$\boldsymbol{F}'_{diff}$	$\boldsymbol{F}'_{vd}$	$\boldsymbol{F}'_{bl}$	$\boldsymbol{F}'_{int}$	$\boldsymbol{F}'_{ext}$	β
I	X	X	X	X	X	depth-dependent
II	X		X			constant
III	X		X			depth-dependent
IV	X	X	X			depth-dependent
V	X	X	X	X		depth-dependent

TABLE 2. Overview of the various experiments.

In this expression, ${F^i}'_{diff}$ is the classical diffusive sediment flux, ${F^i}'_{vd}$ is the sediment flux induced by depth variations, ${F^i}'_{bl}$ is the bedload flux, ${F^i}'_{int}$ is the sediment flux due to internally generated overtides and ${F^i}'_{ext}$ is the flux related to the externally prescribed tide. For explicit expressions of these flux contributions, see Appendix C. Using (3.2) and (3.8), it immediately follows that

$$\omega \hat{h}_n = -({F^1}'_x + l_n {F^2}'). \tag{3.10}$$

The continuity, vorticity and concentration equations (in leading order, $O(\epsilon)$ and $O(\gamma)$, together with the bottom evolution equation (3.10) and the boundary conditions (see Appendix B) define an eigenvalue problem that is solved using a pseudo-spectral method. The elements of the state vector $\Psi'_n = (u^{0,0}_{n,s}, u^{0,0}_{n,c}, v^{0,0}_{n,s}, u^{0,0}_{n,c}, \langle C^{0,0}_n \rangle, C^{0,0}_{n,s2}, C^{0,0}_{n,c2}, \langle u^{1,0}_n \rangle, u^{1,0}_{n,s2}, u^{1,0}_{n,c2}, \langle v^{1,0}_n \rangle, v^{1,0}_{n,s2}, v^{1,0}_{n,c2}, C^{1,0}_{n,s}, C^{1,0}_{n,c}, u^{0,1}_{n,s2}, u^{0,1}_{n,c2}, C^{0,1}_{n,s}, C^{0,1}_{n,c}, \hat{h}_n)$ are expanded in Chebyshev polynomials (see Boyd 2001 for details). Defining $\Psi = (\Psi'_{n,1}, \Psi'_{n,2}, \ldots, \Psi'_{n,N})$ where N is the number of collocation points and $\Psi'_{n,i}$ is Ψ'_n evaluated at the collocation point i, a set of algebraic equations is found:

$$\omega \boldsymbol{B} \Psi = \boldsymbol{A} \Psi. \tag{3.11}$$

The operator $\boldsymbol{A}$ is a $22N \times 22N$ matrix with elements that depend on the lateral wavenumber l_n and the (dimensionless) parameters given in table 1. The $22N \times 22N$ matrix $\boldsymbol{B}$ has non-zero elements only in the lower-right $N \times N$ block, corresponding to the long-time evolution of the bottom.

The solutions of this eigenvalue problem are obtained using standard numerical techniques. It was found that 80 Chebychev polynomials sufficed to get accurate results. The main characteristics of the resulting eigenfunctions Ψ, eigenvalues ω and their dependence on system parameters and the lateral wavenumber l_n is the subject of the next section.

4. Model results

4.1. *Linear stability using default values*

For the default experiment (Experiment I in table 2), parameter values characteristic for the Ameland Inlet system are taken (see the Introduction and table 1). The morphodynamic equilibrium Ψ_{eq} consists of a laterally uniform equilibrium bed profile, sediment concentrations and velocity profiles. The equilibrium bed profile is shown as a solid black line in figure 3(a). In calculating this equilibrium, all components of the sediment flux $\boldsymbol{F}'$ were taken into account.

The results concerning the linear stability of this morphodynamic equilibrium are shown in figure 3(b). Here the dimensionless growth rate Re(ω) (y-axis) is given for different values of the lateral wavenumber l_n (x-axis) and different values of the

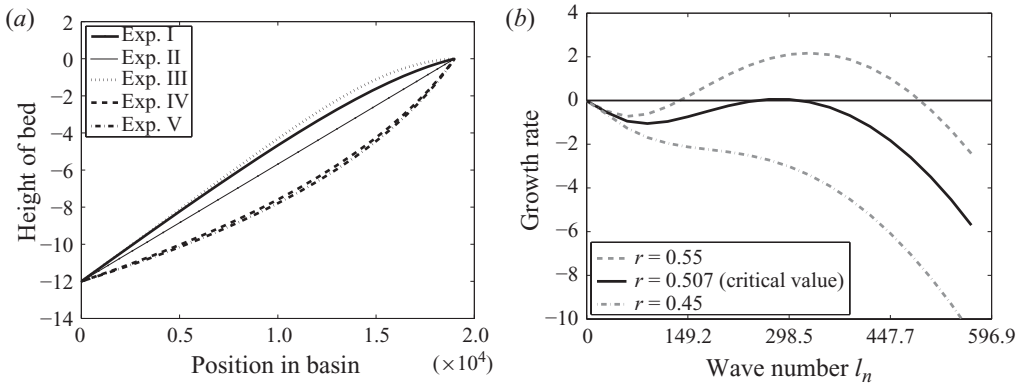

FIGURE 3. Basic state and pattern growth. (*a*) Equilibrium bed profiles. Experiment I is the default case. (*b*) The first longitudinal growth rate for different values of r for the default case.

friction parameter. A dimensionless growth rate of $\omega = 1$ corresponds to an e-folding time scale of $\sim$17.5 years. If bottom perturbations characterized by their wavenumber n have a positive growth rate, they will grow; otherwise their amplitude will decrease. For a critical bottom friction $r_{cr} \sim 0.507$, the underlying one-dimensional equilibrium is neutrally stable. This means that there is one mode (in this case the first longitudinal mode with lateral wavenumber 9) with a vanishing growth rate, i.e. this perturbation neither grows nor decays in time. The bottom pattern of the corresponding eigenmode is shown in figure 5(*a*). The bed perturbations are found at the landward side of the tidal basin. In figure 3(*b*) the growth rates for this critical bottom friction are given by the black solid line, the dashed and dashed-dotted lines show the growth rates for the values of the bottom friction parameters that are respectively larger and smaller than the critical value. This information can be shown in a condensed form by plotting the neutral stability curve: on the x-axis the parameter l_n is shown and on the y-axis the friction parameter. For every l_n, there is a value of the friction parameter for which the first mode in the longitudinal direction, characterized by the wavenumber n, is neutrally stable. This results in the neutral stability curve, shown in figure 4(*a*) as the solid black line. Above the curve the amplitudes of some perturbations grow in time; below they all decay. In this figure the critical friction parameter and the critical value of l_n (in this case l_9) are indicated as r_{cr}^{I} and $l_{n,cr}^{\mathrm{I}}$, respectively.

4.2. *Influence of sediment fluxes*

For the default experiment in the previous section, all sediment flux contributions were taken into account (i.e. $\boldsymbol{F}' = \boldsymbol{F}'_{diff} + \boldsymbol{F}'_{vd} + \boldsymbol{F}'_{bl} + \boldsymbol{F}'_{int} + \boldsymbol{F}'_{ext}$). Here the influence of the various fluxes on the linear stability is shown. The bed perturbations are always located at the landward side, independent of the combination of sediment fluxes. Four different flux combinations are considered and explained below.

The simplified diffusive case (II). In this case only diffusive fluxes and bedload fluxes are considered: $\boldsymbol{F}' = \boldsymbol{F}'_{diff} + \boldsymbol{F}'_{bl}$. Furthermore, β is taken constant. The underlying bed profile is given by the thin solid line in figure 3(*a*). The neutral stability curve for this case is the thin solid line in figure 4(*a*). It is found that the critical friction parameter is much lower than in the default experiment ($r_{cr}^{\mathrm{II}} \sim 0.2$). Furthermore, the most unstable mode has a much lower wavenumber ($l_{n,cr}^{\mathrm{II}} \sim 70$) than in the default case. These results are similar to those found in Schuttelaars & de Swart (1999). However, the corresponding bottom pattern is very different: in our model the bed

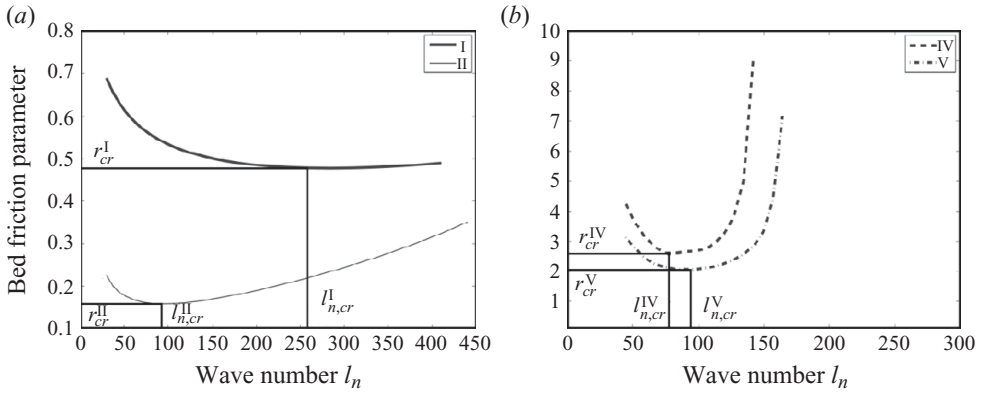

FIGURE 4. Neutral stability curves for the various experiments. (*a*) Experiments I and II. (*b*) Experiments IV and V.

forms are found at the landward side, in the other models they occur in the middle of the tidal basin.

The diffusive case (III). The flux contribution is the same as in the previous case ($\boldsymbol{F}' = \boldsymbol{F}'_{diff} + \boldsymbol{F}'_{bl}$), but the deposition parameter depends on the local water depth. The equilibrium bed profile corresponding to this case is given by the dotted line in figure 3(*a*). Now the underlying equilibrium bed profiles are always unstable for the parameter values used, independent of the bottom friction parameter. Hence there is no critical friction parameter.

The diffusive case including the topographically induced fluxes (IV). This flux is given by $\boldsymbol{F}' = \boldsymbol{F}'_{diff} + \boldsymbol{F}'_{vd} + \boldsymbol{F}'_{bl}$. The morphodynamic equilibrium corresponding to this case is given by the dashed line in figure 3(*a*). The neutral stability curve is given by the dashed line in figure 4(*b*). It is clear that the value of the bottom friction parameter necessary to obtain channels and shoals is much higher than in the default case. Only for very large values of the friction parameter ($r_{cr}^{\mathrm{IV}} \sim 3$), bed perturbations will grow. The wavenumbers of the modes are centred around $l_{n,cr}^{\mathrm{IV}} = 100$.

The combined advective and diffusive case, with only the internally generated advective sediment flux (V). The fluxes contributing to this case are $\boldsymbol{F}' = \boldsymbol{F}'_{diff} + \boldsymbol{F}'_{vd} + \boldsymbol{F}'_{bl} + \boldsymbol{F}'_{int}$. The equilibrium bed profile is presented in figure 3(*a*) as the dashed-dotted line. The influence of the internally generated advective sediment fluxes on the underlying equilibrium and the neutral stability curve (dashed lines in figures 3*a* and 4*b*, respectively) is very small. The underlying profile is slightly more unstable resulting in a slightly lower critical value for the friction parameter.

5. Discussion

5.1. *Instability mechanism*

For the default case, using a friction parameter $r = 0.51$ slightly larger than its critical value r_{cr}^{I}, the most unstable perturbation has a lateral mode number $n = 9$. The corresponding bed perturbation is shown in figure 5(*a*). Taking $y \sim 900$ m (i.e. the solid line in figure 5*a*), the longitudinal structure of the bottom perturbation (dotted solid line) and the corresponding divergences of the sediment fluxes are shown in figure 6(*a*). The divergences of the diffusive and topographically induced sediment fluxes are represented by the solid line and the dashed line, respectively. The

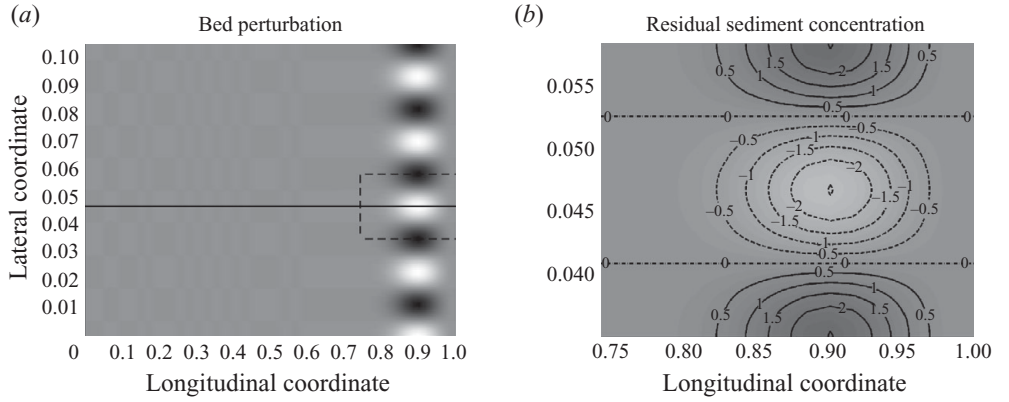

FIGURE 5. Contour plot of (*a*) the scaled bed perturbation, with dark (light) colours a negative (positive) amplitude of the bed perturbation. (*b*) Contour plot of the scaled residual sediment concentration of the most unstable eigenfunction (with lateral mode number $n = 9$) for friction parameter $r = 0.51$ in the region indicated by the dashed box in (*a*). The scaled bed perturbation is shown in greyscales. Other parameter values are given in table 1. A dimensionless sediment concentration of 1 corresponds to a dimensional concentration of $0.15\,\mathrm{kg\ m^{-2}}$.

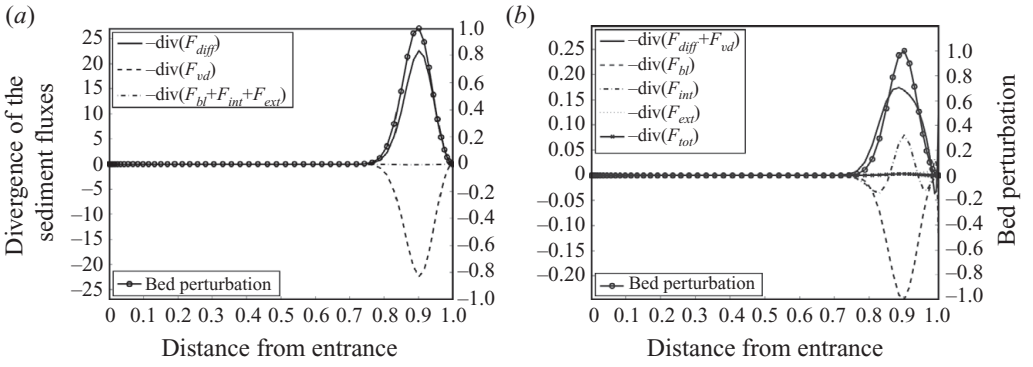

FIGURE 6. Convergence of the sediment fluxes for $n = 9$ and $r = 0.51$. Other parameter values are given in table 1. The dimensionless maximum bottom perturbation is scaled to 1, the fluxes are calculated using this scaled bed perturbation. (*a*) Convergences of all sediment fluxes. (*b*) Convergences of the different sediment fluxes, with $-\nabla \cdot F_{diff}$ and $-\nabla \cdot F_{vd}$ combined.

dashed-dotted line shows the sum of the divergence of the bedload flux, the advective fluxes resulting from internal nonlinear interactions and those due to externally prescribed overtides. The divergences of $\boldsymbol{F}'_{diff}$ and $\boldsymbol{F}'_{vd}$ are much larger than those of the remaining fluxes, but of opposite sign. The classical diffusive flux $\boldsymbol{F}'_{diff}$ enhances the bed perturbation, and the sediment flux $\boldsymbol{F}'_{vd}$ reduces this bed perturbation. In figure 6(*b*) the same divergences are shown again, but now $\boldsymbol{F}'_{diff}$ and $\boldsymbol{F}'_{vd}$ are combined and denoted by the solid line. From now on this sum will be called the total diffusive contribution. Obviously, the diffusive flux is destabilizing, the bedload flux is stabilizing, the internally generated advective flux $\boldsymbol{F}'_{int}$ is mainly destabilizing and the externally generated advective flux $\boldsymbol{F}'_{ext}$ does not play an appreciable role in the growth and decay of the bed forms. In the remainder of this section only the

diffusive fluxes and the internally generated fluxes will be discussed in detail, as the bedload flux is always stabilizing and the flux $\boldsymbol{F}'_{ext}$ is negligible.

5.1.1. *Classical and topographically induced diffusive flux*

From figure 6(*a*) it follows that the classical diffusive flux contributes significantly to the destabilization of the underlying morphodynamic equilibrium. This flux is driven by gradients of the depth-integrated perturbed residual sediment concentration $\langle C_n^{0,0}\rangle$, see figure 5(*b*) for a contour plot. Higher (lower) perturbed residual concentrations are present where the bottom perturbation is negative (positive). This results in a residual diffusive sediment flux from locations where the bottom perturbation is negative to those with a positive bottom perturbation, thus enhancing the instability. The spatial structure of the residual sediment concentration is mainly a result of a balance between the two depositional contributions, one proportional to the perturbed residual concentration and the other to the perturbed deposition parameter β: $\beta_{eq}^{0,0}\langle C_n^{0,0}\rangle \approx -\beta_n^{0,0} C_{eq}^{0,0}\hat{h}_n$ (see Appendix B for details). Since $\beta_n^{0,0}/\beta_{eq}^{0,0} \sim \lambda\beta_{eq}^{0,0}$ at the landward side of the basin (where $h_{eq} \sim 1$), one finds

$$\left\langle C_n^{0,0}\right\rangle \approx -\lambda\beta_{eq}^{0,0} C_{eq}^{0,0}\hat{h}_n. \tag{5.1}$$

Hence a destabilizing diffusive flux $-a\kappa\nabla\cdot < C_n^{0,0} >$ is found. However, a similar contribution, but with opposite sign, is found for the topographically induced sediment flux (see term II in (C 2)). It turns out that the magnitude of this term is slightly larger than the dominant contribution of the classical diffusive flux obtained from (5.1). Hence the sum of these contributions is stabilizing.

Therefore, to understand the *destabilizing* effect of the total diffusive flux, we have to analyse the remaining contributions to the classical diffusive flux. The only other significant contribution to the perturbed residual sediment concentration is due to the erosion of sediment $\langle u_{eq,s}^{0,0} u_{n,s}^{0,0}\rangle$, resulting in

$$\left\langle C_n^{0,0}\right\rangle \approx \left\langle u_{eq,s}^{0,0} u_{n,s}^{0,0}\right\rangle / \beta_{eq}^{0,0}. \tag{5.2}$$

If the perturbed residual concentration $\langle C_n^{0,0}\rangle$ is positive (negative) above a negative (positive) bottom perturbation, the associated classical diffusive flux is destabilizing. Whether this is the case depends on the correlation between $u_{eq,s}^{0,0}$ and $u_{n,s}^{0,0}$. This correlation follows from a delicate balance between frictional effects and continuity: if friction is strong enough, there is a destabilizing flux (for details, see Schuttelaars & de Swart 1999) and this frictional mechanism results in sediment convergence at locations with positive bottom perturbations. As the dominant contribution of the diffusive flux together with the topographically induced flux is stabilizing, bed perturbations will only start to grow if the frictional torques are strong enough to overcome this stabilizing effect.

5.1.2. *Internally generated advective fluxes*

From figure 6(*b*) it follows that the advective sediment flux contributions F_{int}, resulting from the internally generated overtides and residual velocities, are destabilizing at the location of maximum bed perturbation (dashed-dotted line). This flux can be decomposed into seven different contributions, see (C 4). A careful analysis of these terms reveals that the residual sediment transport due to settling lag effects (term II), i.e. the correlation between the equilibrium M_2 velocity $u_{eq,s}^{0,0}$ and the perturbed M_2 concentration $C_{n,s}^{1,0}$, is dominant. This is in contrast to the findings of van Leeuwen (2002) who found that the contribution proportional to the

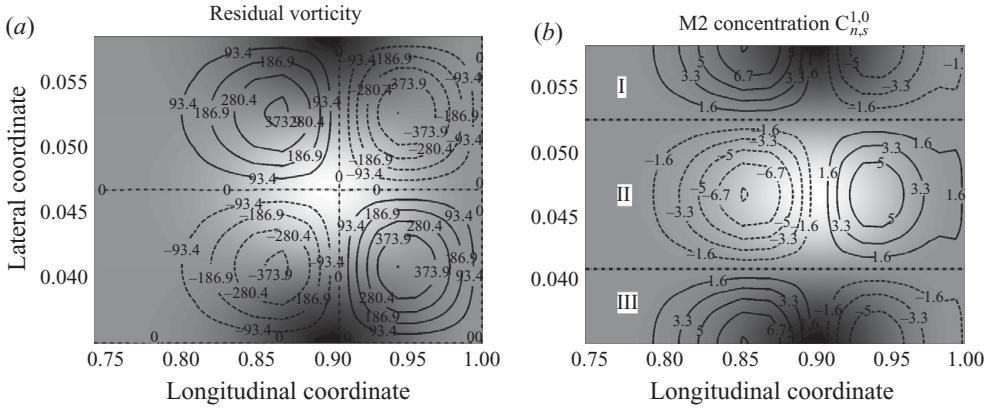

FIGURE 7. Contour plot of the residual vorticity (*a*) and perturbed M_2 concentration $C^{1,0}_{n,s}$ (*b*) for $n=9$ and $r=0.51$; for other parameters, see table 1. The maximum amplitude of the bed perturbation is scaled to 1 and shown in greyscales, with dark (light) colours a negative (positive) amplitude of the bed perturbation. (*a*) Contour plot of the residual vorticity. Positive values indicate a counter-clockwise residual circulation and negative values a clockwise circulation. (*b*) Contour plot of the perturbed M_2 concentration $C^{1,0}_{n,s}$ during ebb.

residual current was dominant. The perturbed concentration $C^{1,0}_{n,s}$ mainly results from a balance between erosion and deposition,

$$\beta^{0,0}_{eq} C^{1,0}_{n,s} \sim 2u^{0,0}_{eq} \left\langle u^{1,0}_{n} \right\rangle . \tag{5.3}$$

The structure of the residual velocity $< u^{1,0}_{n} >$ follows from the residual vorticity balance (see Appendix D), which shows an approximate balance between the divergence of the transfer of tidal vorticity by the tidal M_2 equilibrium velocity and the dissipation of residual vorticity:

$$r \frac{\left\langle \Omega^{1,0}_{n} \right\rangle}{1 - h_{eq} + h_0} \sim - \left\langle u^{0,0}_{eq,s} \Omega^{0,0}_{n,s} \right\rangle_x . \tag{5.4}$$

Here $\langle \Omega^{1,0}_{n} \rangle = \langle v^{1,0}_{n,x} \rangle - \langle u^{1,0}_{n,y} \rangle$ is the residual vorticity and $\Omega^{0,0}_{n,s} = \partial_x v^{0,0}_{n,s} - \partial_y u^{0,0}_{n,s}$ is the M_2 sine component of the leading-order vorticity. The resulting residual vorticity pattern is shown in figure 7(*a*), where solid (dashed) lines indicate counter-clockwise (clockwise) circulation. The generation of the residual circulation cells is a result of the 'tidal rectification mechanism', which is explained in detail by van Leeuwen & de Swart (2001). Using the perturbed residual longitudinal velocity $\langle u^{1,0}_{n} \rangle$, which follows directly from the residual vorticity, and (5.3), the M_2 tidal concentration $C^{1,0}_{n,s}$ can be constructed (see figure 7*b* for this concentration during ebb). As the equilibrium tidal velocity is negative during ebb, it follows that in region II of figure 7(*b*) the advective sediment flux $u^{0,0}_{eq,s} C^{1,0}_{n,s}$ is in the positive x-direction seaward of the maximum of the bed perturbation and in the negative x-direction landward of this position. Hence there is a deposition of sediment at this location and the amplitude of the bed perturbation increases. As both the signs of the M_2 tidal concentration $C^{1,0}_{n,s}$ and the equilibrium tidal flow $u^{0,0}_{eq,s}$ change during flood conditions, this flux is also destabilizing during flood, resulting in a tidally averaged convergence of the advective sediment flux. In a similar way it can be shown that there is a tidally averaged divergence of sediment in regions I and III.

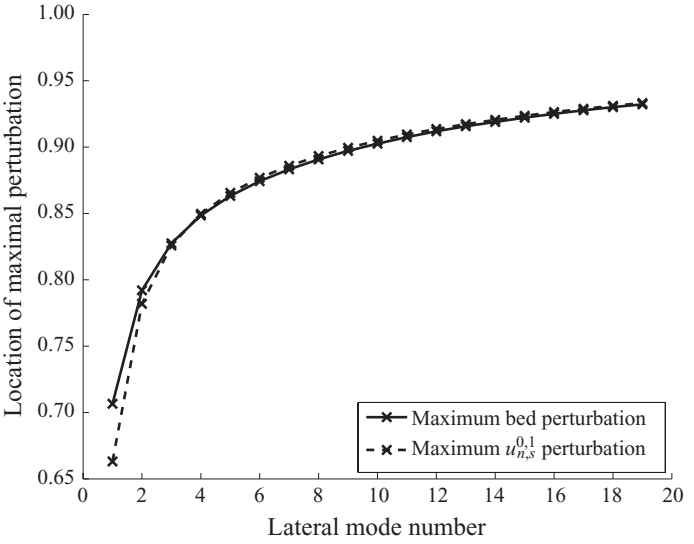

FIGURE 8. Longitudinal location of maximal bed and M_2 velocity perturbation for a varying lateral mode number n and $r = 0.51$. Other parameter values are given in table 1.

5.1.3. *Mode number sensitivity*

From figure 3(b), it follows that only for lateral wavenumbers $n = 9$ and $n = 10$ the bed perturbations have a positive growth rate. The internally generated advective fluxes are always destabilizing, the externally forced advective fluxes are always negligible and the bedload fluxes are always destabilizing (not shown). For small wavenumbers ($n < 5$), the perturbations decay as both the diffusive and the bedload flux are stabilizing. The amplitudes of perturbations with large wavenumbers ($n > 10$) decay due to the stabilizing effect of bedload fluxes. For intermediate wavenumbers, there is a delicate balance between the various fluxes, resulting in either growth or decay of bed forms.

5.2. *Location of maximal bed perturbation*

For both destabilizing mechanisms, it is essential that the perturbed along-channel M_2 velocity decreases (increases) over shallower (deeper) parts. As the largest perturbed concentrations and concentration differences in the lateral direction are found at locations where the perturbed longitudinal M_2 velocity is maximal, the largest bottom perturbations are expected at these locations as well. Hence the position of the largest bottom perturbation is related to the location of the maximum perturbation of the longitudinal M_2 velocity.

For large wavenumbers in the lateral direction, the perturbed velocity $u^{0,1}_{n,s}$ can be written as

$$u^{0,1}_{n,s} = \frac{r^2}{r^2 + (1 - x + h_0)^2} \frac{1}{(1 - x + h_0)} \hat{h}_n, \tag{5.5}$$

which shows that the position of the maximum of $u^{1,0}_{n,s}$ is independent of the bed friction parameter (and independent of h_0 if the balances described in the previous section are still the dominant ones), and is always located at the landward boundary. As the bed perturbation has to vanish at the landward boundary, it is expected that the maxima of bottom perturbations are found near the landward end. This is confirmed in figure 8, which shows the locations of the maximum perturbed

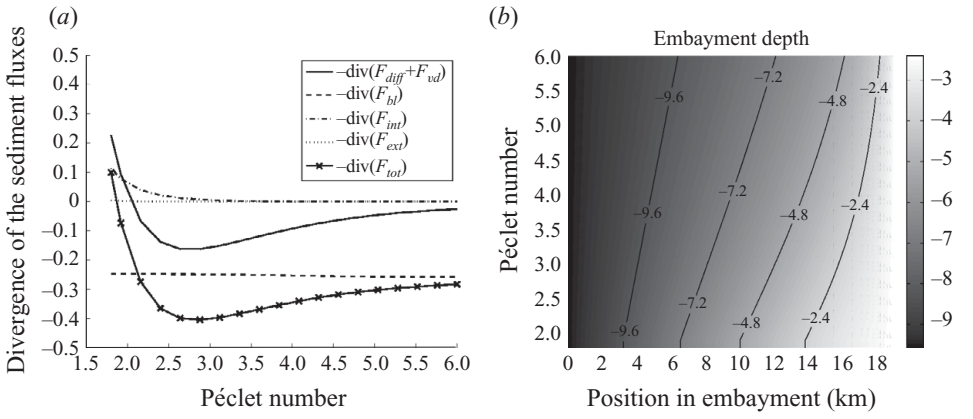

FIGURE 9. The influence of the sediment settling velocity (Péclet number) on the convergences of the sediment fluxes (*a*) and the underlying one-dimensional equilibrium bed profile (*b*). Other parameter values are given in table 1.

along-channel M_2 velocity and the maximum bed perturbation for different values of lateral wavenumber n.

5.3. *Parameter sensitivity*

In this section the sensitivity of the model results will be investigated by varying the settling velocity w_s, the phase ϕ between the prescribed M_2 and M_4 sea surface elevation at the entrance and the parameter h_0 that is used to normalize the bottom friction.

5.3.1. *Settling velocity and external phase*

By varying the settling velocity w_s between 1.5 cm s^{-1} (fine sand) and 5 cm s^{-1} (medium sand), the sediment Péclet number $\lambda = w_s H/\kappa_v$ is varied between 1.8 and 6, and the parameter a between 0.06 and 0.006. Variations in the parameter a only have a minor influence on the stability properties of the underlying morphodynamic equilibrium, whereas changes in the Péclet number strongly influence these properties. Taking the mode number $n = 9$, the convergences of the resulting sediment fluxes are shown in figure 9(*a*) for the varying Péclet number at the location where the (normalized) perturbed bed is maximal. For the sediment Péclet number smaller than approximately 2, the underlying width-averaged morphodynamic equilibrium is unstable, with increasing growth rates for the decreasing Péclet number. When increasing the Péclet number, the underlying morphodynamic equilibrium is stable. As the approximate balances and mechanisms discussed in § 5.1 are still applicable, the influence of the Péclet number on the stability of the underlying equilibrium can be understood: the underlying equilibrium bottom becomes deeper at the end of the basin for the increasing sediment Péclet number, see figure 9(*b*). Hence the frictional effects are weaker for larger Péclet numbers, resulting in weaker destabilizing fluxes and hence the laterally uniform morphodynamic equilibria are stable for a larger Péclet number.

The externally prescribed phase difference is varied between $165^\circ \leqslant \phi \leqslant 198^\circ$: for $\phi \leqslant 187^\circ$ the morphodynamic equilibrium is stable, and for larger phase differences it becomes unstable. The dependence of the stability of the underlying morphodynamic equilibrium on the phase angle can again be attributed to the changes in the underlying morphodynamic equilibrium: for larger phase angles, the equilibrium bed becomes

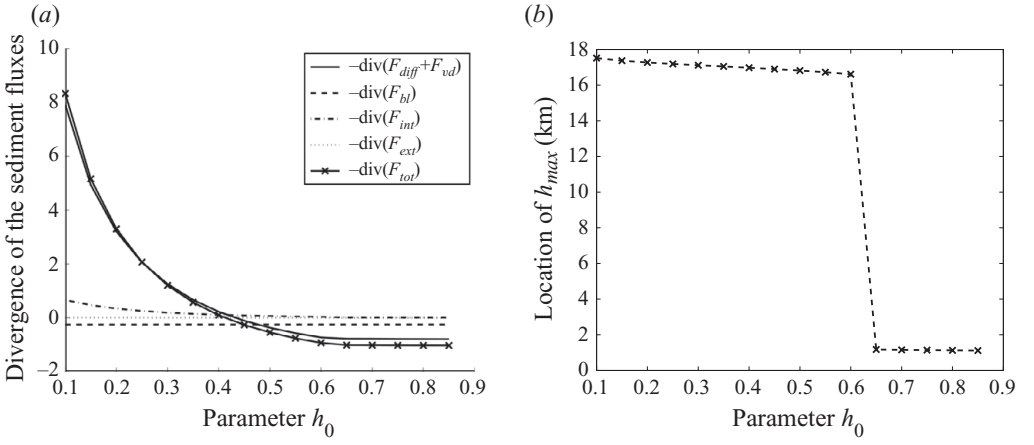

FIGURE 10. The influence of the parameter h_0 on the convergences of the sediment fluxes (a) and the longitudinal location of the maximal bed perturbation (b). Other parameter values are given in table 1.

shallower, resulting in stronger destabilizing fluxes. If the equilibrium bed is too deep at the end of the embayment, the destabilizing fluxes are too small and the laterally uniform equilibrium is stable.

5.3.2. *Bottom friction parametrization*

In the formulation for the bottom friction, a parameter h_0 was introduced to regularize the bottom friction contribution. In figure 10(a), the divergences of the sediment fluxes are shown for h_0 varied between 0.1 and 0.85. For small h_0, the underlying equilibrium is linearly unstable. Smaller values of h_0 result in larger growth rates as the frictional effects become stronger. For $h_0 > 0.45$, the equilibrium bed profile becomes stable: in this case friction is not strong enough anymore to overcome the damping effects of continuity, and hence the bed perturbations decay. Note that for $h_0 > 0.6$ the bed perturbations, which are stable, are not found at the end of the embayment anymore (see figure 10b), but near the entrance. This is not in contradiction with the discussion in § 5.2 as the main balance for the residual concentration is completely different: in this case there is mainly a balance between diffusive and depositional contributions, resulting in a maximum bed perturbation at the seaward side. As the *unstable* modes are always found at the landward side of the embayment (this was tested for different parameter settings), this balance will not be discussed in detail here. If h_0 becomes large, the approach taken in Schuttelaars & de Swart (1999) and van Leeuwen & de Swart (2004) is satisfactory, and a detailed discussion of the balances can be found in these articles, see also ter Brake & Schuttelaars (2009).

5.4. *Influence of sediment transport contributions*

When considering only diffusive ($\boldsymbol{F}'_{diff}$) and bedload ($\boldsymbol{F}'_{bl}$) fluxes, using a constant deposition parameter β (case II), a small value of the bottom friction parameter suffices to make the bed perturbations grow. If the deposition parameter β depends on local depth (case III), no bed friction is needed for the bed perturbations to grow. This difference follows from a different balance for the residual perturbed

concentration $\langle C_n^{0,0} \rangle$. Its main balance reads (see (B 9))

$$\beta_{eq}^{0,0} \langle C_n^{0,0} \rangle = -\beta_n^{1,0} \hat{h}_n \langle C_{eq}^{0,0} \rangle + u_{n,s}^{0,0} u_{s,eq}^{0,0}. \tag{5.6}$$

If the deposition parameter β depends on local depth, the term on the left-hand side is balanced by the first term on the right-hand side. The perturbed concentration is proportional to minus the bed perturbation, resulting in a destabilizing contribution, independent of the value of the bottom friction parameter. If this contribution is larger than the stabilizing bedload contribution, the morphodynamic equilibrium is unstable. In the case of a constant deposition parameter, $\beta_n^{1,0}$ is zero and there is an approximate balance between the remaining terms. Now frictional effects are essential for instability; see the discussion of the mechanism in § 5.1.2.

The other cases (IV and V) follow directly from the discussion of the default case. The main differences can be explained by the fact that the underlying morphodynamic equilibria change considerably due to the inclusion/exclusion of different suspended sediment fluxes.

6. Conclusions

In this paper the linear stability of laterally uniform morphodynamic equilibria in short, rectangular tidal basins is investigated using an idealized model. It is shown that these equilibria are linearly unstable if a critical value of the bottom friction parameter is exceeded, resulting in the initial formation of channels and shoals at the landward side of the basin.

The instability mechanism is clarified by a detailed study of the various contributions to the sediment flux. The divergence of the diffusive sediment flux and the topographically induced sediment flux are dominant but of opposite sign. The difference results in a small destabilizing contribution if the friction parameter is large enough. In that case, frictional torques cause the tidal velocities to decrease over shoals and increase in the channels, resulting in a destabilizing diffusive sediment flux. This mechanism was already discussed by Schuttelaars & de Swart (1999). Apart from this mechanism, the advective sediment flux, resulting from internally generated overtides, is destabilizing as well. Externally prescribed overtides do not contribute significantly to the (de)stabilizing sediment fluxes. The main contribution of the internally generated advective sediment transport is due to settling lag effects, i.e. the correlation between the equilibrium M_2 velocity and the perturbed M_2 concentration.

The initial formation of channels and shoals is always found at the landward side of the embayment. Schuttelaars & de Swart (1999) found global modes with a maximum in the middle of the basin, whereas van Leeuwen & de Swart (2001) found that with increasing influence of advective fluxes (with respect to diffusive fluxes) the preferred location of the bottom perturbations shifts from the middle of the basin towards the basin entrance. These differences in model results can be explained by observing that Schuttelaars & de Swart (1999) and van Leeuwen & de Swart (2001, 2004) use a linear approximation of the bottom friction in the momentum equations, while the generally accepted formulation of this contribution is retained in this paper.

Investigation of the sensitivity of the model results to sediment flux formulation shows that the main differences between the results obtained with different sediment flux formulations can be attributed to changes in the underlying morphodynamic equilibria. This observation is also applicable to variations in parameter values: the

mechanisms resulting in instabilities are robust for a wide range of parameters, and differences in growth rates can be attributed to changes in the *underlying* morphodynamic equilibria.

In formulating the model, various simplifications were made such as the neglect of Coriolis and wind effects, and the critical velocity for erosion. Furthermore, drying and flooding at the landward side were not modelled explicitly. However, the initial formation of channels and shoals at the landward side of tidal embayments is supported by results obtained with fully nonlinear numerical models (van der Wegen & Roelvink 2008): initial bed perturbations start to grow at the landward side and then extend towards the entrance of the embayment. This evolution is clearly a result of nonlinear interactions which are not accounted for in the present paper, making a comparison of model results with observational data and equilibrium solutions of complex numerical models not very useful at this point. However, as the perturbations resemble the observed initial channel–shoal systems obtained in complex numerical models, it is expected that a fully nonlinear idealized model will capture the observed long-term behaviour. Such a nonlinear model is developed and presently under investigation.

Appendix A. The linearized equations

Considering the momentum equation, substituting ζ and only retaining terms that are linear in the small perturbation, yields $\zeta'_x = \zeta'_y = 0$. Using the boundary condition for ζ at the entrance, it follows that $\zeta' = 0$. Hence, there are no perturbations in the sea level ζ, i.e. $\zeta' = 0$ everywhere.

Substituting (3.1) into equations (2.11), (2.15), (2.16) and (2.17), using $\zeta' = 0$ and only retaining terms that are linear in the perturbation, yields the following system of equations:

$$[(\epsilon\zeta_{eq} + 1 - h_{eq})u' - h'u_{eq}]_x + [(\epsilon\zeta_{eq} + 1 - h_{eq})v']_y = 0, \tag{A 1a}$$

$$[v'_x - u'_y]_t + \epsilon[u_{eq}v'_x - u_{eq}u'_y]_x = -\left[\frac{rv'}{1 - h_{eq} + \epsilon\zeta + h_0}\right]_x + \frac{ru_{eq}(h')_y}{(1 - h_{eq} + \epsilon\zeta + h_0)^2} + \left[\frac{ru'}{1 - h_{eq} + \epsilon\zeta + h_0}\right]_y, \tag{A 1b}$$

$$aC'_t + a[\epsilon u_{eq}C' + \epsilon u'C_{eq} - \kappa C'_x - \kappa\lambda(\beta_{eq}h_{eq\,x}C' + \beta_{eq}h'_xC_{eq} + \beta' h_{eq\,x}C_{eq})]_x + [\epsilon v'C_{eq} - \kappa C'_y - \kappa\lambda\beta_{eq}h'_yC_{eq}]_y = 2u_{eq}u' - (\beta_{eq}C' + \beta' C_{eq}), \tag{A 1c}$$

$$h'_\tau = -\langle \nabla \cdot \boldsymbol{F}' \rangle, \tag{A 1d}$$

where the perturbed flux contributions are given by

$$F^{1'} = a\epsilon\,\langle u_{eq}C' + u'C_{eq}\rangle - a\kappa\,\langle C'\rangle_x - a\kappa\lambda\langle\beta_{eq}h_{eq\,x}C' + \beta_{eq}h'_xC_{eq} + \beta' h_{eq\,x}C_{eq}\rangle - \mu h'_x, \tag{A 2}$$

$$F^{2'} = a\epsilon\,\langle v'C_{eq}\rangle - a\kappa\,\langle C'\rangle_y - a\kappa\lambda\langle\beta_{eq}h_{eq\,y}C' + \beta_{eq}h'_yC_{eq}\rangle - \mu h'_y, \tag{A 3}$$

and the equilibrium and perturbed deposition parameter by

$$\beta_{eq} = [1 - \exp[-\lambda(\epsilon\zeta + 1 - h_{eq})]]^{-1} \quad \text{and} \quad \beta' = \frac{\lambda \exp[-\lambda\left(\epsilon\zeta + 1 - h_{eq}\right)]}{\left(1 - \exp[-\lambda\left(\epsilon\zeta + 1 - h_{eq}\right)]\right)^2} h' \tag{A 4}$$

The linearized boundary conditions at the seaward side $x = 0$ read

$$h' = 0, \quad v' = 0, \quad \beta_{eq}\langle C'\rangle + \beta'\langle C_{eq}\rangle = u_{eq}u', \quad \tilde{C}'(x, y, t, \kappa) = \tilde{C}'(x, y, t, \kappa = 0), \tag{A 5}$$

at the sidewalls $y = 0, \boldsymbol{B}$ they are given by

$$\mu h'_y = 0, \quad v' = 0, \quad -\kappa C'_y - \kappa\lambda\beta_{eq}h'_y C_{eq} = 0, \tag{A 6}$$

and at the landward boundary $x = 1$ by

$$\left.\begin{aligned} &h' = 0, \quad -h_{eq,x}u' - u_{eq}h'_x + \epsilon\zeta_{eq}u'_x + \epsilon\zeta_{eq}v'_y = 0, \quad \tilde{C}'(x, y, t, \kappa) = \tilde{C}'(x, y, t, \kappa = 0), \\ &a\epsilon\langle u_{eq}C' + u'C_{eq}\rangle - a\kappa\langle C'\rangle_x - a\kappa\lambda\langle\beta_{eq}h_{eq_x}C' + \beta_{eq}h'_x C_{eq} + \beta' h_{eq_x}C_{\mathrm{eq}}\rangle - \mu h'_x = 0. \end{aligned}\right\} \tag{A 7}$$

Appendix B. The Eigenvalue problem: final equations

The linearized deposition parameter $\beta = \beta_{eq} + \beta'$ with β_{eq} and β' given in (A 4), is expanded as follows:

$$\beta_{eq} = \beta_{eq}^{0,0} + \epsilon\beta_{eq}^{1,0}, \quad \beta' = \beta_n^{0,0}h' + \epsilon\beta_n^{1,0}h', \tag{B 1}$$

with

$$\left.\begin{aligned} &\beta_{eq}^{0,0} = [1 - \exp[-\lambda(1 - h_{eq})]]^{-1}, \quad \beta_{eq}^{1,0} = -\lambda \exp^{-\lambda(1-h_{eq})}\beta_{eq}^{0,0^2}, \\ &\beta_n^{0,0} = \lambda \exp[-\lambda(1 - h_{eq})]\beta_{eq}^{0,0^2}, \quad \beta_n^{1,0} = \lambda^2 \exp[-\lambda(1 - h_{eq})] \\ &\qquad \times(1 + \exp[-\lambda(1 - h_{eq})])[-1 + \exp[-\lambda(1 - h_{eq})]]^{-3}. \end{aligned}\right\} \tag{B 2}$$

The $O(1)$ continuity equation reads

$$\left.\begin{aligned} \sim \cos(t) \quad &-\frac{\mathrm{d}}{\mathrm{d}x}h_{eq}u_{n,c}^{0,0} + (1 - h_{eq})\left(\frac{\mathrm{d}}{\mathrm{d}x}u_{n,c}^{0,0} + l_n v_{n,c}^{0,0}\right) = 0, \\ \sim \sin(t) \quad &-\frac{\mathrm{d}}{\mathrm{d}x}h_{eq}u_{n,s}^{0,0} - \frac{\mathrm{d}}{\mathrm{d}x}\hat{h}_n u_{eq,s}^{0,0} + (1 - h_{eq})\left(\frac{\mathrm{d}}{\mathrm{d}x}u_{n,s}^{0,0} + l_n v_{n,s}^{0,0}\right) - \hat{h}_n\frac{\mathrm{d}}{\mathrm{d}x}u_{eq,s}^{0,0} = 0, \end{aligned}\right\} \tag{B 3}$$

and the vorticity equation is given by

$$\left.\begin{aligned} \sim \cos(t) \quad &\frac{\mathrm{d}}{\mathrm{d}x}v_{n,s}^{0,0} + l_n u_{n,s}^{0,0} = -r\frac{\mathrm{d}}{\mathrm{d}x}\left[\frac{v_{n,c}^{0,0}}{1 + h_0 - h_{eq}}\right] - rl_n\frac{u_{n,c}^{0,0}}{1 + h_0 - h_{eq}}, \\ \sim \sin(t) \quad &-\frac{\mathrm{d}}{\mathrm{d}x}v_{n,c}^{0,0} - l_n u_{n,c}^{0,0} = -r\frac{\mathrm{d}}{\mathrm{d}x}\left[\frac{v_{n,s}^{0,0}}{1 + h_0 - h_{eq}}\right] \\ &-rl_n\frac{u_{n,s}^{0,0}}{1 + h_0 - h_{eq}} - rl_n\frac{u_{eq,s}^{0,0}\hat{h}_n}{(1 + h_0 - h_{eq})^2}. \end{aligned}\right\} \tag{B 4}$$

The $O(1)$ time-varying concentration equation reads

$$\left.\begin{aligned} &\sim \cos(2t) && 2aC^{0,0}_{n,s2} + akC^{0,0}_{n,c2}l_n^2 + \beta^{0,0}_{eq}C^{0,0}_{n,c2} + \beta^{1,0}_{n}\hat{h}_nC^{0,0}_{n,c2} + u^{0,0}_{eq,s}u^{0,0}_{n,s} = 0,\\ &\sim \sin(2t) && -2aC^{0,0}_{n,c2} + akC^{0,0}_{n,s2}l_n^2 + \beta^{0,0}_{eq}C^{0,0}_{n,s2} + \beta^{1,0}_{n}\hat{h}_nC^{0,0}_{eq,s2} - u^{0,0}_{eq,s}u^{0,0}_{n,c} = 0. \end{aligned}\right\} \tag{B 5}$$

The $O(\epsilon)$ continuity equation becomes

$$\left.\begin{aligned} &\sim \text{const.} && \frac{\mathrm{d}}{\mathrm{d}x}\left[(1-h_{eq})\left\langle u^{1,0}_n\right\rangle\right] + (1-h_{eq})\left\langle v^{1,0}_n\right\rangle l_n = -\frac{1}{2}\frac{\mathrm{d}}{\mathrm{d}x}u^{0,0}_{n,c} - \frac{1}{2}l_nv^{0,0}_{n,c},\\ &\sim \cos(2t) && \frac{\mathrm{d}}{\mathrm{d}x}\left[(1-h_{eq})u^{1,0}_{n,c2}\right] + (1-h_{eq})v^{1,0}_{n,c2}l_n = -\frac{1}{2}\frac{\mathrm{d}}{\mathrm{d}x}u^{0,0}_{n,c} - \frac{1}{2}l_nv^{0,0}_{n,c},\\ &\sim \sin(2t) && \frac{\mathrm{d}}{\mathrm{d}x}\left[(1-h_{eq})u^{1,0}_{n,s2}\right] - \frac{\mathrm{d}}{\mathrm{d}x}\left[\hat{h}_nu^{1,0}_{eq,s2}\right] + (1-h_{eq})v^{1,0}_{n,s2}l_n\\ &&& \quad = -\frac{1}{2}\frac{\mathrm{d}}{\mathrm{d}x}u^{0,0}_{n,s} - \frac{1}{2}l_nv^{0,0}_{n,s}, \end{aligned}\right\} \tag{B 6}$$

and $O(\epsilon)$ vorticity equation reads

$$\left.\begin{aligned} &\sim \text{const.} && \frac{1}{2}\frac{\mathrm{d}}{\mathrm{d}x}\left[u^{0,0}_{eq,s}l_nu^{0,0}_{n,s}\right] + \frac{1}{2}\frac{\mathrm{d}}{\mathrm{d}x}\left[u^{0,0}_{eq,s}\frac{\mathrm{d}}{\mathrm{d}x}v^{0,0}_{n,s}\right] = -r\frac{\mathrm{d}}{\mathrm{d}x}\left[\frac{\left\langle v^{1,0}_n\right\rangle}{1+h_0-h_{eq}}\right]\\ &&& \quad -r\frac{\left\langle u^{1,0}_n\right\rangle l_n}{(1+h_0-h_{eq})^2} + \frac{1}{2}rl_n\frac{u^{0,0}_{n,c}\zeta_{eq,c}}{(1+h_0-h_{eq})^2} + \frac{1}{2}r\frac{\frac{\mathrm{d}}{\mathrm{d}x}v^{0,0}_{n,c}\zeta_{eq,c}}{(1+h_0-h_{eq})^2},\\ &\sim \cos(2t) && 2\frac{\mathrm{d}}{\mathrm{d}x}v^{1,0}_{n,s2} + 2u^{1,0}_{n,s2}l_n - \frac{1}{2}\frac{\mathrm{d}}{\mathrm{d}x}\left[u^{0,0}_{eq,s}l_nu^{0,0}_{s}\right] - \frac{1}{2}\frac{\mathrm{d}}{\mathrm{d}x}\left[u^{0,0}_{eq,s}\frac{\mathrm{d}}{\mathrm{d}x}v^{0,0}_{n,s}\right]\\ &&& \quad = -\frac{\mathrm{d}}{\mathrm{d}x}\left[\frac{rv^{1,0}_{n,c2}}{1+h_0-h_{eq}}\right] + \frac{1}{2}r\frac{\mathrm{d}}{\mathrm{d}x}\left[\frac{v^{0,0}_{n,c}\zeta_{eq,c}}{(1+h_0-h_{eq})^2}\right]\\ &&& \quad\quad + \frac{1}{2}rl_n\frac{u^{0,0}_{n,c}\zeta_{eq,c}}{(1+h_0-h_{eq})^2} - rl_n\frac{u^{1,0}_{n,c2}}{1+h_0-h_{eq}},\\ &\sim \sin(2t) && -2\frac{\mathrm{d}}{\mathrm{d}x}v^{1,0}_{n,c2} - 2u^{1,0}_{n,c2}l_n + \frac{1}{2}\frac{\mathrm{d}}{\mathrm{d}x}\left[u^{0,0}_{eq,s}l_nu^{0,0}_{n,c}\right] + \frac{1}{2}\frac{\mathrm{d}}{\mathrm{d}x}\left[u^{0,0}_{eq,s}\frac{\mathrm{d}}{\mathrm{d}x}v^{0,0}_{n,c}\right]\\ &&& \quad = -\frac{\mathrm{d}}{\mathrm{d}x}\left[\frac{rv^{1,0}_{n,s2}}{1+h_0-h_{eq}}\right] + \frac{1}{2}r\frac{\mathrm{d}}{\mathrm{d}x}\left[\frac{v^{0,0}_{n,s}\zeta_{eq,c}}{(1+h_0-h_{eq})^2}\right]\\ &&& \quad\quad + \frac{1}{2}rl_n\frac{u^{0,0}_{n,s}\zeta_{eq,c}}{(1+h_0-h_{eq})^2} - rl_n\frac{u^{1,0}_{n,s2}}{1+h_0-h_{eq}} - rl_n\frac{u^{1,0}_{eq,s2}\hat{h}_n}{(1+h_0-h_{eq})^2}\\ &&& \quad\quad + rl_n\frac{u^{0,0}_{eq,s}\zeta^c_{eq}\hat{h}_n}{1+h_0-h_{eq}}. \end{aligned}\right\} \tag{B 7}$$

The $O(\epsilon)$ concentration equation reads

$$\left.\begin{aligned}
\sim \cos(t)\quad & aC^{1,0}_{n,s} + \beta^{0,0}_{eq}C^{1,0}_{n,c} - u^{0,0}_{eq,s}u^{1,0}_{n,s2} + \frac{1}{2}a\frac{\mathrm{d}}{\mathrm{d}x}\left[u^{0,0}_{eq,s}C^{0,0}_{n,s2}\right] \\
& + a\frac{\mathrm{d}}{\mathrm{d}x}\left[u^{0,0}_{n,c}\left\langle C^{0,0}_{eq}\right\rangle + \frac{1}{2}u^{0,0}_{n,s}C^{0,0}_{eq,s2} + \frac{1}{2}u^{0,0}_{n,c}C^{0,0}_{eq,c2}\right] \\
& + al_n\left[v^{0,0}_{n,c}\left\langle C^{0,0}_{eq}\right\rangle + \frac{1}{2}v^{0,0}_{n,c}C^{0,0}_{eq,c2} + \frac{1}{2}v^{0,0}_{n,s}C^{0,0}_{eq,s2}\right] \\
& + \beta^{1,0}_{n}\hat{h}_n\left(\left\langle C^{0,0}_{eq}\right\rangle + \frac{1}{2}C^{0,0}_{eq,c2}\right) + \beta^{1,0}_{eq}\left(\left\langle C^{0,0}_{n}\right\rangle + \frac{1}{2}C^{0,0}_{n,c2}\right) \\
& + \beta^{1,0}_{n}\hat{h}_nC^{1,0}_{eq,c} - u^{1,0}_{eq,s2}u^{0,0}_{n,s} = 0, \\
\sim \sin(t)\quad & -aC^{1,0}_{n,c} + \beta^{0,0}_{eq}C^{1,0}_{n,s} - 2u^{0,0}_{eq,s}u^{1,0} + u^{0,0}_{eq,s}u^{1,0}_{n,c2} \\
& + a\frac{\mathrm{d}}{\mathrm{d}x}\left[u^{0,0}_{eq,s}\left(\left\langle C^{0,0}_{n}\right\rangle - \frac{1}{2}C^{0,0}_{n,c2}\right)\right] \\
& + a\left\{\frac{\mathrm{d}}{\mathrm{d}x}\left[u^{0,0}_{s}\left(\left\langle C^{0,0}_{eq}\right\rangle - \frac{1}{2}C^{0,0}_{eq,c2}\right)\right] + \frac{1}{2}\frac{\mathrm{d}}{\mathrm{d}x}\left[u^{0,0}_{n,c}C^{0,0}_{eq,s2}\right]\right\} \\
& + al_n\left[v^{0,0}_{n,s}\left(\left\langle C^{0,0}_{eq}\right\rangle - \frac{1}{2}C^{0,0}_{eq,c2}\right) + \frac{1}{2}v^{0,0}_{n,c}C^{0,0}_{eq,s2}\right] \\
& + \frac{1}{2}\beta^{1,0}_{n}\hat{h}_nC^{0,0}_{eq,s2} + \beta^{1,0}_{eq}\frac{1}{2}C^{0,0}_{n,s2} + \beta^{1,0}_{n}\hat{h}_nC^{1,0}_{eq,s} - u^{1,0}_{eq,s2}u^{0,0}_{n,c} = 0,
\end{aligned}\right\} \tag{B 8}$$

and the time mean concentration component follows from

$$\left.\begin{aligned}
\sim \text{const.}\quad & -ak\frac{\mathrm{d}}{\mathrm{d}x}\left[\frac{\mathrm{d}}{\mathrm{d}x}C^{0,0}_{n} + \lambda\beta^{0,0}_{eq}\left(\frac{\mathrm{d}}{\mathrm{d}x}h_{eq}\left\langle C^{0,0}_{n}\right\rangle + \frac{\mathrm{d}}{\mathrm{d}x}\hat{h}_n\left\langle C^{0,0}_{eq}\right\rangle\right)\right. \\
& \left. + \lambda\beta^{0,0}_{n}\hat{h}_n\frac{\mathrm{d}}{\mathrm{d}x}h_{eq}\left\langle C^{0,0}_{eq}\right\rangle\right] - ak\left[-\left\langle C^{0,0}_{n}\right\rangle l_n^2 - \lambda\beta^{0,0}_{eq}\left\langle C^{0,0}_{eq}\right\rangle\hat{h}_nl_n^2\right] \\
& + \beta^{0,0}_{eq}\left\langle C^{0,0}_{n}\right\rangle + \beta^{0,0}_{n}\hat{h}_n\left\langle C^{0,0}_{eq}\right\rangle - u^{0,0}_{eq,s}u^{0,0}_{n,s} + \frac{1}{2}a\epsilon^2u^{0,0}_{eq,s}\frac{\mathrm{d}}{\mathrm{d}x}C^{1,0}_{n,s} \\
& + a\epsilon^2\left[\frac{\mathrm{d}}{\mathrm{d}x}\left\langle u^{1,0}_{n}C^{0,0}_{eq}\right\rangle + l_n\left\langle v^{1,0}_{n}C^{0,0}_{eq}\right\rangle\right] \\
& + \frac{1}{2}a\epsilon^2\left[\frac{\mathrm{d}}{\mathrm{d}x}\left(u^{1,0}_{n,c2}C^{0,0}_{eq,c2}\right) + \frac{\mathrm{d}}{\mathrm{d}x}\left(u^{1,0}_{n,s2}C^{0,0}_{eq,s2}\right)\right. \\
& \left. + l_n\left(v^{1,0}_{n,c2}C^{0,0}_{eq,c2} + v^{1,0}_{n,s2}C^{0,0}_{eq,s2}\right)\right] = 0.
\end{aligned}\right\} \tag{B 9}$$

The $O(\gamma)$ continuity equation reads

$$\left.\begin{aligned}
\sim \cos(2t)\quad & \frac{\mathrm{d}}{\mathrm{d}x}\left[(1-h_{eq})u^{0,1}_{n,c2} - \hat{h}_nu^{0,1}_{eq,c2}\right] + l_n(1-h_{eq})v^{0,1}_{n,c2} = 0, \\
\sim \sin(2t)\quad & \frac{\mathrm{d}}{\mathrm{d}x}\left[(1-h_{eq})u^{0,1}_{n,s2} - \hat{h}_nu^{0,1}_{n,s2}\right] + l_n(1-h_{eq})v^{0,1}_{n,s2} = 0,
\end{aligned}\right\} \tag{B 10}$$

and the vorticity equation reads

$$\left.\begin{aligned}
\sim \cos(2t) \quad & 2\frac{\mathrm{d}}{\mathrm{d}x}v_{n,s2}^{0,1} + 2l_n u_{n,s2}^{0,1} = -r\frac{\mathrm{d}}{\mathrm{d}x}\left[\frac{v_{n,c2}^{0,1}}{1+h_0-h_{eq}}\right] - rl_n\frac{u_{n,c2}^{0,1}}{1+h_0-h_{eq}} \\
& -rl_n\frac{u_{eq,c2}^{0,1}\hat{h}_n}{(1+h_0-h_{eq})^2}, \\
\sim \sin(2t) \quad & -2\frac{\mathrm{d}}{\mathrm{d}x}v_{n,c2}^{0,1} - 2l_n u_{n,c2}^{0,1} = -r\frac{\mathrm{d}}{\mathrm{d}x}\left[\frac{v_{n,s2}^{0,1}}{1+h_0-h_{eq}}\right] - rl_n\frac{u_{n,s2}^{0,1}}{1+h_0-h_{eq}} \\
& -rl_n\frac{u_{eq,s2}^{0,1}\hat{h}_n}{(1+h_0-h_{eq})^2}.
\end{aligned}\right\} \quad \text{(B 11)}$$

The $O(\gamma)$ concentration components follow from

$$\left.\begin{aligned}
\sim \cos(t) \quad & aC_{n,s}^{0,1} - u_{eq,s}^{0,0}u_{n,s2}^{0,1} - u_{n,s}^{0,0}u_{eq,s2}^{0,1} - u_{n,c}^{0,0}u_{eq,c2}^{0,1} + \beta_{eq}^{0,0}C_{n,c}^{0,1} + \beta_n^{1,0}\hat{h}_n C_{eq,c}^{0,1}, \\
\sim \sin(t) \quad & a\left(-C_{n,c}^{0,1}\right) + u_{eq,s}^{0,0}u_{n,c2}^{0,1} + u_{n,s}^{0,0}u_{eq,c2}^{0,1} + u_{n,c}^{0,0}u_{eq,s2}^{0,1} + \beta_{eq}^{0,0}C_{n,s}^{0,1} + \beta_n^{1,0}\hat{h}_n C_{eq,s}^{0,1}.
\end{aligned}\right\} \quad \text{(B 12)}$$

Finally, the bed evolution equation reads

$$\omega\hat{h}_n = -[F_x^{1'} + l_n F^{2'}], \quad \text{(B 13)}$$

with the components of () defined in Appendix C. The boundary conditions at $x=0$ are given by

$$\left.\begin{aligned}
O(1): \quad & \hat{h}_n = 0, \quad v_{n,s}^{0,0} = 0, \quad v_{n,c}^{0,0} = 0, \\
& \beta_{eq}\left\langle C_n^{0,0}\right\rangle + \beta_n^{1,0}\hat{h}_n\left\langle C_{eq}^{0,0}\right\rangle - u_{\mathrm{eq,s}}^{0,0}u_{n,s}^{0,0} = 0, \\
O(\epsilon): \quad & r\left\langle v_n^{1,0}\right\rangle + \frac{1}{2}u_{eq,s}^{0,0}\frac{\mathrm{d}}{\mathrm{d}x}v_{n,s}^{0,0} = 0, \quad -2v_{n,c2}^{1,0} + \frac{1}{2}u_{eq,s}^{0,0}\frac{\mathrm{d}}{\mathrm{d}x}v_{n,c}^{0,0} + rv_{n,s2}^{1,0} = 0, \\
& 2v_{n,s2}^{1,0} - \frac{1}{2}u_{eq,s}^{0,0}\frac{\mathrm{d}}{\mathrm{d}x}v_{n,s}^{0,0} + rv_{n,c2}^{1,0} = 0, \\
O(\gamma): \quad & v_{n,c2}^{0,1} = 0, \quad v_{n,s2}^{0,1} = 0.
\end{aligned}\right\} \quad \text{(B 14)}$$

The boundary conditions at $x=1$ are

$$\left.\begin{aligned}
O(1): \quad & \hat{h}_n = 0, \quad F^1 = 0, \quad -\frac{\mathrm{d}}{\mathrm{d}x}h_{eq}u_{n,s}^{0,0} - \frac{\mathrm{d}}{\mathrm{d}x}\hat{h}_n u_{eq,s}^{0,0} = 0, \quad u_{n,c}^{0,0} = 0, \\
O(\epsilon): \quad & -\frac{\mathrm{d}}{\mathrm{d}x}h_{eq}\left\langle u_n^{1,0}\right\rangle + \frac{1}{2}\frac{\mathrm{d}}{\mathrm{d}x}u_{n,c}^{0,0} + \frac{1}{2}l_n v_{n,c}^{0,0} = 0, \quad -\frac{\mathrm{d}}{\mathrm{d}x}h_{eq}u_{n,c2}^{1,0} + \frac{1}{2}u_{n,c,x}^{0,0} \\
& + \frac{1}{2}l_n v_{n,c}^{0,0} = 0 \\
& -\frac{\mathrm{d}}{\mathrm{d}x}h_{eq}u_{n,s2}^{1,0} + \frac{1}{2}\frac{\mathrm{d}}{\mathrm{d}x}u_{n,s}^{0,0} + \frac{1}{2}l_n v_{n,s}^{0,0} - \frac{\mathrm{d}}{\mathrm{d}x}\hat{h}_n u_{eq,s2}^{1,0} = 0, \\
O(\gamma): \quad & -\frac{\mathrm{d}}{\mathrm{d}x}h_{eq}u_{n,c2}^{0,1} - \frac{\mathrm{d}}{\mathrm{d}x}\hat{h}_n u_{eq,c2}^{0,1} = 0, \quad -\frac{\mathrm{d}}{\mathrm{d}x}h_{eq}u_{n,s2}^{0,1} - \frac{\mathrm{d}}{\mathrm{d}x}\hat{h}_n u_{eq,s2}^{0,1} = 0.
\end{aligned}\right\} \quad \text{(B 15)}$$

Appendix C. Sediment flux components

The various flux components in the x- and y-directions are as follows:

$$\boldsymbol{F}_{diff} = \left(-a\kappa \left\langle \frac{\mathrm{d}}{\mathrm{d}x} C_n^{0,0} \right\rangle, a\kappa l_n \left\langle C_n^{0,0} \right\rangle\right), \tag{C 1}$$

$$\boldsymbol{F}_{vd} = \left(-a\kappa\lambda \left[\beta_{eq}^{0,0} \left(\underbrace{\left\langle C_n^{0,0} \right\rangle \frac{\mathrm{d}}{\mathrm{d}x} h_{eq}}_{\text{term I}} + \underbrace{\frac{\mathrm{d}}{\mathrm{d}x} \hat{h}_n \left\langle C_{eq}^{0,0} \right\rangle}_{\text{term II}} \right) + \underbrace{\beta_n^{1,0} \left(\hat{h}_n \frac{\mathrm{d}}{\mathrm{d}x} h_{eq} \left\langle C_{eq}^{0,0} \right\rangle \right)}_{\text{term III}} \right], a\kappa\lambda \beta_{eq}^{0,0} \hat{h}_n \left\langle C_{eq} \right\rangle l_n \right), \tag{C 2}$$

$$\boldsymbol{F}_{bl} = \left(-\mu \frac{\mathrm{d}}{\mathrm{d}x} \hat{h}_n, \mu l_n \hat{h}_n\right). \tag{C 3}$$

The internally generated advective contribution $\boldsymbol{F}_{M2} = (F_{M2}^1, F_{M2}^2)$ has components given by

$$\left.\begin{aligned} F_{M2}^1 &= \frac{1}{2} a\epsilon^2 \left(\underbrace{C_{n,s}^{1,0} u_{eq}^{0,0}, s}_{\text{term I}} + \underbrace{2\left\langle u_n^{1,0} C_{eq}^{0,0} \right\rangle}_{\text{term II}} + \underbrace{u_{n,c2}^{1,0} C_{\mathrm{eq,c2}}^{0,0}}_{\text{term III}} + \underbrace{u_{n,s2}^{1,0} C_{\mathrm{eq,s2}}^{0,0}}_{\text{term IV}} + \underbrace{u_{n,s}^{0,0} C_{eq,s}^{1,0}}_{\text{term V}} \right. \\ &\quad \left. + \underbrace{u_{n,c}^{0,0} C_{eq,c}^{1,0}}_{\text{term VI}} + \underbrace{C_{n,s2}^{0,0} u_{eq,s2}^{1,0}}_{\text{term VII}} \right), \\ F_{M2}^2 &= \frac{1}{2} \epsilon^2 a \left(\underbrace{2\left\langle v_n^{1,0} C_{eq}^{0,0} \right\rangle}_{\text{term II}} + \underbrace{v_{n,c2}^{1,0} C_{eq,c2}^{0,0}}_{\text{term III}} + \underbrace{v_{n,s2}^{1,0} C_{eq,s2}^{0,0}}_{\text{term IV}} + \underbrace{v_{n,s}^{0,0} C_{eq,s}^{1,0}}_{\text{term V}} + \underbrace{v_{n,c}^{0,0} C_{eq,c}^{1,0}}_{\text{term VI}} \right), \end{aligned}\right\} \tag{C 4}$$

and the advective contribution due to externally prescribed overtides $\boldsymbol{F}_{M4} = (F_{M4}^1, F_{M4}^2)$ has components given by

$$\left.\begin{aligned} F_{M4}^1 &= \frac{1}{2} a\epsilon\gamma \left(\underbrace{C_{n,s}^{0,1} u_{eq,s}^{0,0}}_{\text{term I}} + \underbrace{u_{n,s}^{0,0} c_{eq,s}^{0,1}}_{\text{term II}} + \underbrace{u_{n,c}^{0,0} C_{eq,c}^{0,1}}_{\text{term III}} + \underbrace{u_{n,s2}^{0,1} C_{eq,s2}^{0,0}}_{\text{term IV}} + \underbrace{u_{n,c2}^{0,1} C_{eq,c2}^{0,0}}_{\text{term V}} \right. \\ &\quad \left. + \underbrace{C_{n,s2}^{0,0} u_{eq,s2}^{0,1}}_{\text{term VI}} + \underbrace{C_{n,c2}^{0,0} u_{eq,c2}^{0,1}}_{\text{term VII}} \right), \\ F_{M4}^2 &= \frac{1}{2} a\epsilon\gamma \left(\underbrace{v_{n,s}^{0,0} C_{eq,s}^{0,1}}_{\text{term II}} + \underbrace{v_{n,c}^{0,0} C_{eq,c}^{0,1}}_{\text{term III}} + \underbrace{v_{n,s2}^{0,1} C_{eq,s2}^{0,0}}_{\text{term IV}} + \underbrace{v_{n,c2}^{0,1} C_{eq,c2}^{0,0}}_{\text{term V}} \right). \end{aligned}\right\} \tag{C 5}$$

Appendix D. Vorticity equation

The relative vorticity is given by

$$\Omega = \Omega_{eq} + \Omega', \quad \text{with } \Omega' = v'_x - u'_y. \tag{D 1}$$

Substituting the solutions for u and v from (3.2) together with the expression for $\hat{u}_n(x,t)$ and $\hat{v}_n(x,t)$, as stated in § 3, into the expression for Ω' gives

$$\begin{aligned}\Omega' = &\left[v^{0,0}_{n,c}\cos(t) + v^{0,0}_{n,s}\sin(t) + \epsilon\left(\langle v^{1,0}_n\rangle + v^{1,0}_{n,c2}\cos(2t) + v^{1,0}_{n,s2}\sin(2t)\right)\right]_x \\ &+\left[u^{0,0}_{n,c}\cos(t) + u^{0,0}_{n,s}\sin(t) + \epsilon\left(\langle u^{1,0}_n\rangle + u^{1,0}_{n,c2}\cos(2t) + u^{1,0}_{n,s2}\sin(2t)\right)\right]_y \qquad \text{(D 2a)} \\ = &\left[\frac{\mathrm{d}}{\mathrm{d}x}v^{0,0}_{n,c}\cos(t) + \frac{\mathrm{d}}{\mathrm{d}x}v^{0,0}_{n,s}\sin(t) - \frac{\mathrm{d}}{\mathrm{d}y}u^{0,0}_{n,c}\cos(t) - \frac{\mathrm{d}}{\mathrm{d}y}u^{0,0}_{n,s}\sin(t)\right] \\ &+\epsilon\left[\left\langle\frac{\mathrm{d}}{\mathrm{d}x}v^{1,0}_n\right\rangle + \left\langle\frac{\mathrm{d}}{\mathrm{d}y}u^{1,0}_n\right\rangle\right] + \epsilon[\text{internally generated } \mathrm{M}_4 \text{ terms}]. \qquad \text{(D 2b)}\end{aligned}$$

Following the expression of the solutions as stated in (3.2), Ω' can be written as

$$\Omega' = \mathrm{Re}\{\hat{\Omega}_n(x,t)\cos(l_n y)\,\mathrm{e}^{\omega\tau}\}, \tag{D 3}$$

where

$$\hat{\Omega}_n(x,t) = \Omega^{0,0}_n(x,t) + \epsilon\Omega^{1,0}_n(x,t) + \cdots. \tag{D 4}$$

Combining the expressions above yields

$$\Omega^{0,0}_n = \underbrace{\left(\frac{\mathrm{d}}{\mathrm{d}x}v^{0,0}_{n,c} - \frac{\mathrm{d}}{\mathrm{d}y}u^{0,0}_{n,c}\right)}_{\Omega^{0,0}_{n,c}}\cos(t) + \underbrace{\left(\frac{\mathrm{d}}{\mathrm{d}x}v^{0,0}_{n,s} - \frac{\mathrm{d}}{\mathrm{d}y}u^{0,0}_{n,s}\right)}_{\Omega^{0,0}_{n,s}}\sin(t), \tag{D 5a}$$

$$\langle\Omega^{1,0}_n\rangle = \left\langle\frac{\mathrm{d}}{\mathrm{d}x}v^{1,0}_n\right\rangle + \left\langle\frac{\mathrm{d}}{\mathrm{d}y}u^{1,0}_n\right\rangle. \tag{D 5b}$$

In order to understand the spatial pattern of $\langle u^{1,0}_n\rangle$, an expression for the M_2 vorticity component $\langle\Omega^{1,0}_n\rangle$ needs to be found. Therefore the time-averaged $O(\epsilon)$ equation for vorticity is considered:

$$\begin{aligned}\frac{\mathrm{d}}{\mathrm{d}x}\left\langle u^{0,0}_{n,s}\Omega^{0,0}_{n,s} + u^{0,0}_{n,c}\Omega^{0,0}_{n,c}\right\rangle + \frac{\mathrm{d}}{\mathrm{d}y}\left\langle v^{0,0}_{n,s}\Omega^{0,0}_{n,s} + v^{0,0}_{n,c}\Omega^{0,0}_{n,c}\right\rangle &= \frac{-r\left\langle\Omega^{1,0}_n\right\rangle}{(1-h+h_0)} \\ &- r\frac{\left\langle v^{1,0}_n\right\rangle\frac{\mathrm{d}}{\mathrm{d}x}h_{eq} + \left\langle u^{1,0}_n\right\rangle\frac{\mathrm{d}}{\mathrm{d}y}h_{eq}}{(1-h_{eq}+h_0)^2}. \qquad \text{(D 6)}\end{aligned}$$

Eliminating the equilibrium solution and neglecting the nonlinear terms in the perturbations gives

$$r\frac{\left\langle\Omega^{1,0}_n\right\rangle}{(1-h_{eq}+h_0)} = -\frac{\mathrm{d}}{\mathrm{d}x}\left[u^{0,0}_{eq,s}\left(\frac{\mathrm{d}}{\mathrm{d}x}v^{0,0}_{n,s} - u^{0,0}_{n,s\,y}\right)\right] - r\frac{\left\langle v^{1,0}_n\right\rangle\frac{\mathrm{d}}{\mathrm{d}x}h_{eq}}{(1-h_{eq}+h_0)^2}. \tag{D 7}$$

It turns out that the last term on the left-hand side is negligible compared to the other terms in this expression.

REFERENCES

Boyd, J. P. 2001 *Chebyshev and Fourier Spectral Methods*. Mineola.

ter Brake, M. C. & Schuttelaars, H. M. 2009 Influence of bottom friction formulation on the initial formation of channels in a short tidal embayment. In *River, Coastal and Estuarine*

Morphodynamics 2009 (ed. C. Vionnet, M. Garcia, A. Latrubesse & G. Perillo), pp. 153–159. Taylor & Francis.

TER BRAKE, M. C. & SCHUTTELAARS, H. M. 2010 Modeling equilibrium bed profiles of short tidal. On the effect of the vertical distribution of suspended sediment and the influence of the boundary conditions. *Ocean Dyn.* **60**, 183–204.

CLEVERINGA, J. & OOST, A. P. 1999 The fractal geometry of tidal channel systems in the Dutch Wadden Sea. *Geol. Mijnb.* **78**, 21–30.

D'ALPAOS, A., LANZONI, S., MARANI, M. & RINALDO, A. 2007 Landscape evolution in tidal embayments: modeling the interplay of erosion, sedimentation, and vegetation dynamics. *J. Geophys. Res.* **112**, F01008.

DAVIS, R. A. J. 1996 *Coasts*. Prentice Hall.

DE SWART, H. E. & ZIMMERMAN, J. T. F. 2009 Morphodynamics of tidal inlet systems. *Annu. Rev. Fluid Mech.* **41**, 203–229.

DISSANAYAKE, D. M. P. K., ROELVINK, J. A. & VAN DER WEGEN, M. 2009 Modelled channel patterns in a schematized tidal inlet. *Coast. Engng* **56**, 1069–1083.

EHLERS, J. 1988 *The Morphodynamics of the Wadden Sea*. Balkema.

HIBMA, A., SCHUTTELAARS, H. M. & DE VRIEND, H. 2004 Initial formation and evolution of channel–shoal patterns in estuaries. *Cont. Shelf Res.* **24**, 1637–1650.

HIBMA, A., DE VRIEND, H. J. & STIVE, M. J. F. 2003 Numerical modelling of shoal pattern formation in well-mixed elongated estuaries. *Estuar. Coast. Shelf Sci.* **57**, 981–991.

VAN LEEUWEN, S. M. 2002 Tidal inlet systems: bottom pattern formation and outer delta development. PhD thesis, Utrecht University.

VAN LEEUWEN, S. M., SCHUTTELAARS, H. M. & DE SWART, H. E. 2000 Tidal and morphologic properties of embayments: effects of sediment deposition processes and length variation. *Phys. Chem. Earth* B **25**, 365–368.

VAN LEEUWEN, S. M. & DE SWART, H. E. 2001 The effect of advective processes on the morphodynamic stability of short tidal embayments. *Phys. Chem. Earth* B **26**, 735–740.

VAN LEEUWEN, S. M. & DE SWART, H. E. 2004 Effect of advective and diffusive sediment transport on the formation of local and global bottom patterns in tidal embayments. *Ocean Dyn.* **54**, 441–451.

MARANI, M., BELLUCO, E., D'ALPAOS, A., DEFINA, A., LANZONI, S. & RINALDO, A. 2003 On the drainage density of tidal networks. *Water Resour. Res.* **39**, 10–40.

MARCIANO, R., WANG, Z. B., HIBMA, A. & DE VRIEND, H. J. 2005 Modeling of channel patterns in short tidal basins. *J. Geophys. Res.* **110**, F01001.

ROELVINK, J. A. 2006 Coastal morphodynamic evolution techniques. *Coast. Engng* **53**, 277–287.

SCHRAMKOWSKI, G. P., SCHUTTELAARS, H. M. & DE SWART, H. E. 2002 The effect of geometry and bottom friction on local bed forms in a tidal embayment. *Cont. Shelf Res.* **22**, 1821–1834.

SCHUTTELAARS, H. M., SCHRAMKOWSKI, G. P. & DE SWART, H. E. 2001 Initial formation of estuarine sections. In *River, Coastal and Estuarine Morphodynamics*, pp. 443–452. IAHR.

SCHUTTELAARS, H. M. & DE SWART, H. E. 1996 An idealized long-term morphodynamic model of a tidal embayment. *Eur. J. Mech.* B/*Fluids* **15** (1), 55–80.

SCHUTTELAARS, H. M. & DE SWART, H. E. 1999 Initial formation of channels and shoals in a short tidal embayment. *J. Fluid Mech.* **386**, 15–42.

SCHUTTELAARS, H. M. & DE SWART, H. E. 2000 Multiple morphodynamic equilibria in tidal embayments. *J. Geophys. Res.* **105**, 24105–24118.

SHA, L. P. 1989 Cyclic morphological changes of the ebb tidal delta off Texel inlet, The Netherlands. *Geol. Mijnb.* 35–48.

VREUGDENHIL, C. B. 1994 *Numerical Methods for Shallow Water Flow* (Water Sci. & Techn. Libr.). Kluwer.

VAN DER WEGEN, M. & ROELVINK, J. A. 2008 Long-term morphodynamic evolution of a tidal embayment using a two-dimensional process-based model. *J. Geophys. Res.* **7**, C03016.

ZIMMERMAN, J. T. F. 1982 On the Lorentz linearization of a quadratically damped forced oscillator. *Phys. Lett.* **89A**, 123–124.